FINAL REPORT

Inertial/GPS Integrated Geolocation System for Detection and Recovery of Buried Munitions

SERDP Project MR-1565

JULY 2011

Christopher Jekeli
Jong-Ki Lee
Ohio State University

This document has been cleared for public release

SERDP
DOD • EPA • DOE

This report was prepared under contract to the Department of Defense Strategic Environmental Research and Development Program (SERDP). The publication of this report does not indicate endorsement by the Department of Defense, nor should the contents be construed as reflecting the official policy or position of the Department of Defense. Reference herein to any specific commercial product, process, or service by trade name, trademark, manufacturer, or otherwise, does not necessarily constitute or imply its endorsement, recommendation, or favoring by the Department of Defense.

Table of Contents

List of Tables iv
List of Figures v
Acronyms vii
Keywords viii
Acknowledgements ix
Abstract x

1. Introduction 1
1.1 Background 1
1.2 Technical Objectives 1
2. Technology Description 3
2.1 The Kalman Filter 3
2.2. Sampling-Based Filters 4
2.2.1 Unscented Kalman Filter (UKF) 4
2.2.2 Unscented Particle Filter (UPF) 5
2.2.3 Rao-Blackwellized Unscented Particle Filter (RBUPF) 6
2.3 Adaptive Filtering 7
2.3.1 Neural Network Aided Adaptive Filtering 8
2.4 Smoothing 11
2.4.1 Kalman Smoother (KS) 11
2.4.2 Particle Filter Smoothing 12
2.4.3 Rao-Blackwellized Particle Smoother (RBPS) 12
2.5 Wave Correlation Filter 12
2.6 End-Matching 13
3. Filter Simulations 14
3.1 Simulation Setup 14
3.2 Results and Analysis 17
4. Performance Using IMU Data 25
4.1 Static Laboratory Tests 27
4.1.1 Test Description 27
4.1.2 Results and Analysis 27

4.2 Cart-Based Laboratory Tests 30
4.2.1 Test Description 31
4.2.2 Results and Analysis 32
4.3 Hand-Held System Tests 34
4.3.1 Test Description 36
4.3.2 Results and Analysis 37
4.4 Field Tests at NRL Test Facility 39
4.4.1 Test Description 40
4.4.2 Results and Analysis 42
4.5 Self-Calibration Tests 44
4.5.1 Simulation Tests 46
4.5.2 Field Tests 46
4.5.3 Results and Analysis 48
5. Cost Analysis 51
6. Summary and Conclusions 54

Publications reporting the project achievements 56
References 57

List of Tables

Table 1. IMU levels of accuracy.. 14
Table 2. The assumed precision of ranging solutions ..15
Table 3. Statistics of errors (all segments) using nonlinear filters on data from a medium-grade IMU with uniformly distributed errors and with 1 Hz GPS updates (units: cm) 21
Table 4. Noise levels for the IMU accelerometers (static mode) 30
Table 5. Noise levels for the IMU gyros (static mode).. 30
Table 6. The error specification of three IMUs 31
Table 7. Cost comparison of geolocation systems 52

List of Figures

Figure 1. The neuron with three basic elements 10

Figure 2. The generated control path 16

Figure 3. Flow chart of loosely coupled, decentralized ranging/IMU integration and simulation analysis 17

Figure 4. Standard deviation of errors of different IMU grades with 1 s ranging system updates using different filters (first row: curve segments, second row: straight segments, first column: GPS, second column: total station) (units: cm) 18

Figure 5. Standard deviation of errors for different filtering methods (first row: curve segments, second row: straight segments, first column: 10 s, second column: 30 s GPS updates of the medium-grade IMU) (units: cm) 19

Figure 6. Standard deviation of errors with medium-grade IMU and degraded GPS updates and with different scales in the unscented transformation (first row: curve segments, second row: straight segments, first column: GPS 1 sec updates, second column: GPS 5 sec updates) 20

Figure 7. Asymmetric pdf's used for gyro noise ($l = 2$, $a = 0.25$) and accelerometer noise ($l = 2$, $a = 0.75$) 22

Figure 8. Standard deviation of medium-grade IMU position errors with asymmetric sensor error distributions, for baseline-degraded GPS updates (first row: curve segments, second row: straight segments, first column: 1 s updates, second column: 5 s updates) 23

Figure 9. Standard deviations of medium-grade IMU position errors (first row: curved segments, second row: straight segments) for EKF, UKF and UPF with 1 s GPS updates (first column) and for EKF, UKF, UPF[1](200), UPF[2](400), UPF[3](600), AUPF(200) with 5 s updates (second column). The number in parenthesis is the number of particles. GPS update accuracy is for the 1 km baseline (Table 2) and the IMU sensor noise is assumed to be asymmetric as in Figure 7 (units: cm) 24

Figure 10. a) HG1700 IMU, b) HG1900 IMU 25

Figure 11. Manufacturer specifications for HG1700 and HG1900 26

Figure 12. PSD's of the HG1700 (top) and HG1900 (bottom) accelerometers in the static mode 28

Figure 13. PSD's of the HG1700 (top) and HG1900 (bottom) gyros in the static mode 29

Figure 14. Cart Based Geolocation System, Front (A: HG1700 and HG1900 with run-box, B H764G, C: Pin Point Indicator with Mark) 31

Figure 15. Laboratory test trajectory 32

Figure 16. Position Errors of CBGS according to different IMUs and filtering/smoothing methods (control updates every 2 points) 33

Figure 17. Position errors of CBGS according to different IMUs and filtering/smoothing methods (control updates every third point) 33

Figure 18. Position Error of CBGS according to different IMUs and NN aided filtering/smoothing method (control updates every 2 points) 34

Figure 19. Position Error of CBGS according to different IMUs and NN aided filtering/smoothing method (control updates every 3 points) 34

Figure 20. The hardware system for locating geolocation tests (A: Handheld Geolocation System, B: Laptop, C: IMU Run-box, D: Web Cam, E: Target (red dot) with black box, F: HG1900, G: Target tracking software, and H: PCMCIA converter) 35

Figure 21. Target position tracking software 36

Figure 22. The first sweep and swing trajectory from five tests of the designed handheld UXO Geolocation platform 37

Figure 23. The average standard deviations of position errors according to various smoothing methods (unit: cm) for the sweep tests 38

Figure 24. The average standard deviations of position errors according to various smoothing methods (unit: cm) for the swing tests 39

Figure 25. (a) The NRL Multi-sensor Towed Array Detection System (MTADS), (b) IMU box, (c) OSU's dual-IMU/GPS system 40

Figure 26. The NRL cart-based system with OSU's dual-IMU/GPS geolocation system 40

Figure 27. The GPS trajectory of the vehicle-towed trailer and cart-based System (Tests 2 and 5 are Scenario 1 and Tests 6 and 7 are Scenario 2) 41

Figure 28. IMU/GPS Data Processing Flowchart 42

Figure 29. The estimated vehicle trajectory using GPS, the HG1700 w/ UKF the WCF, and end-matching, for different update rates 43

Figure 30. The standard deviation of position error in the straight section according to the UKF, the UKF with WCF, and the UKF with WCF and end-matching based on the UKF solutions (left: Test 2, right: Test 5) 44

Figure 31. The standard deviation of position error in the straight section according to the UKF, the UKF with the wave correlation filter, and the UKF with the wave correlation filter and end-matching based on the UKF solutions (left: Test 6, right: Test 7) 44

Figure 32. Cart-Based Geolocation System with 1) IMU box containing the HG1900 and HG1700; 2) 120 VAC inverter; 3) 12 VDC battery; 4) hand-pulled cart; 5) Trimble NERTS GPS receiver; 6) Trimble Zephyr Geodetic II GPS

antenna; 7) laptop computer, including PCMCI card connecting the IMUs and the decoding software 47

Figure 33. GPS trajectory of field IMU calibration tests 47

Figure 34. HG1700 inertial positioning errors with self-calibrated IMU errors according to different scenarios (see text) compared to the case without any prior self-calibration prior in the field 49

Figure 35. HG1900 inertial positioning errors with self-calibrated IMU errors according to different scenarios (see text) compared to the case without any prior self-calibration prior in the field 50

Acronyms

AEKS	Adaptive EKF Smoothing
AI	Artificial Intelligence
APD	Asymmetric Probability Density
AUKS	Adaptive UKF-RTS Smoothing
AUPF	Adaptive Unscented Particle Filter
CBGS	Cart-Based Geolocation System
DGM	Digital Geophysical Mapping
DGPS	Differential GPS
EKF	Extended Kalman Filter
EMI	Electromagnetic Induction
FBS	Forward-Backward Smoother
GPS	Global Positioning System
HGS	Handheld Geolocation System
IMU	Inertial Measurement Unit
KS	Kalman Smoother
MAP	Maximum a Posteriori
MEC	Munitions and Explosives of Concern
MFN	Multi-layer Feed-forward Network
MTADS	Multi-sensor Towed Array Detection System
NN-AEKS	Neural Network Adaptive Extended Kalman Filter/Smoother
NN-AUKS	Neural Network Adaptive Unscented Kalman Filter/Smoother
NRL	Naval Research Laboratory
pdf	probability density function
PF	Particle Filter
RBPF	Rao-Blackwellized Particle filter
RBPS	Rao-Blackwellized Particle Smoother
RBUPF	Rao-Blackwellized Unscented Particle Filter
RLG	Ring Laser Gyroscopes
RN	Recurrent Network
RTK	Real-Time Kinematic
RTS	Rauch-Tung-Striebel
RTS	Robotic Total Station
SFN	Single-layer Feed-forward Network
SIS	Sequential Importance Sampling
TFS	Two-Filter Smoother
UAV	Unmanned Airborne Vehicle
UKF	Unscented Kalman Filter
UPF	Unscented Particle Filter
UT	Unscented Transformation

UXO	Unexploded Ordnance
WCF	Wave Correlation Filter

Keywords

GPS, INS, Kalman Filter, Adaptive Filter, Unscented Kalman Filter, Particle Filter, Rao-Blackwellized Particle Filter, Neural Network, Wave Correlation, Smoothing, UXO, MEC

Acknowledgments

This research was funded by the SERDP grant MM-1565. Technical support of Dr. Anne Andrews and Dr. Herb Nelson, Munitions Response Program Managers, SERDP&ESTCP, and Mr. Peter F. Knowles and Mr. Daniel Ruedy, SERDP/ESTCP Support Office, is greatly appreciated. We'd like to thank in particular Daniel A. Steinhurst and Glenn R. Harbaugh, both at the Naval Research Laboratory (NRL), for helping conduct our field tests at NRL's UXO test site.

Abstract

The extent of buried munitions and explosives of concern (MEC), or unexploded ordnance (UXO), creates a serious environmental hazard in the U.S., especially where military bases and ranges are being converted to civilian use (millions of acres). The cleanup of these sites presents a formidable challenge to DoD, most prominently in terms of accurate and reliable detection and classification. Discrimination between MEC and relatively safe background clutter (scrap metal) is a monumental problem that depends on the instrument technology, as well as on the processing methodology that inverts the detection data to infer MEC. Reducing the number of false alarms in the detection process can save billions of dollars in the cleanup effort. That process and the consequent savings rely in large part on precise three-dimensional positioning (geolocation) of the detection sensors both to aid in the inversion of the data in post-survey data processing and in the mapping and recovery of locations with positive identification. Although the detection instrument technology has advanced significantly in the last decade, it is often still the geolocation technology that defines or limits the accuracy of MEC detection.

The objective of this project was to develop and test novel geolocation algorithms applied to scenarios typical of MEC detection and recovery, where the precision goals are 1 cm and 10 cm for three-dimensional positioning of magnetic and electro-magnetic detection devices. The principal geolocation system was assumed to be based on inertial measurement units (IMUs) integrated with differential GPS. The GPS receiver presumably is of geodetic quality commensurate with the precision goals and serves as the reference system. The IMUs are tactical-grade, three-dimensional accelerometers and gyroscopes that supplement GPS positioning by a) improving the temporal (hence spatial) resolution; and b) bridging temporary GPS outages or degradations caused by obstructions of the satellite lines-of-sight or caused by other electronic interferences, as well as multi-path effects. A major component is also the calibration of systematic sensor errors using external measurements and information. The resulting techniques and software were tested on ground vehicle and man-portable systems.

Alternatives to the standard extended Kalman filter were developed and tested. Using simulated data, as well as data obtained from actual instrumented systems in the laboratory and in the field, we tested various optimal non-linear filters and smoothers in order to demonstrate the interpolation capabilities of medium-grade IMUs. The unscented Kalman filter performed significantly better than the standard version, particularly over highly dynamic curved segments of the simulated and actual trajectories, yielding up to 50% improvement in the position accuracy. Similar improvement was obtained for the unscented particle filter, and its adaptive variant, over the unscented Kalman filter when the statistical distribution of the IMU noise was non-symmetric (i.e., essentially non-Gaussian). While the few-centimeter geolocation accuracy goal for highly dynamic UXO characterization applications remains a challenge if tactical grade IMUs are integrated with a significantly degraded ranging system, using filters appropriate to the inherent nonlinear dynamics and potential non-Gaussian nature of the sensor noise tend to reduce overall errors compared to the traditional filter.

1. Introduction

1.1 Background

In North America, especially in the US, the problem of unexploded ordnance (UXO) extends beyond military training sites, fields of battle, and military bases. According to the Defense Science Board Task Force on UXO, 15 million acres or more are potentially contaminated at over 1500 different sites (Defense Science Board, 2003). The typical method to find UXO employs time domain electromagnetic induction (EMI) devices that transmit pulsed magnetic fields and then sense the fields produced by induced currents in buried highly conducting objects such as UXO. However, the false alarm rate is often very high and the detection and remediation of UXO in contaminated sites using such detect-and-dig methods is extremely inefficient since it is difficult to distinguish the buried UXO from the noise of geologic magnetic sources or anthropic clutter items such as exploded ordnance fragments and agriculture or industrial artifacts (Bell, 2001). The cost can be as high as $1.4 million/acre (Collins et al., 2001; Zhang et al., 2003). Thus, new aiding technologies that can improve discrimination performance for UXO detection are urgently needed.

Digital Geophysical Mapping (DGM) integrates multiple sensors to detect and characterize potential UXO. However, without highly precise position data DGM is ineffective because the position uncertainty can degrade the inversion of EMI data and the subsequent classification (Tarokh et al., 2004; U.S. Army Corps of Engineers 2006). The requirements of position accuracy for UXO detection fall into three levels; *initial screening* that needs tens of centimeters accuracy as standard deviation, *area mapping* that needs less than 5cm, and *characterization and discrimination* that need less than 2cm accuracy.

The Global Positioning System (GPS) has been used as a precise positioning system specifically for geolocation of UXO detectors. Laser-based ranging, radio, and acoustic ranging have also been considered as alternative positioning methods. All ranging systems perform geolocation by trilateration, which requires unobstructed lines-of-sight and uninterrupted transmission of signals that connect the detector and at least three reference points. From this standpoint, GPS is representative of all ranging systems. However, the temporal resolution of GPS kinematic positioning (1 Hz, typically) is less than for some other systems, such as laser ranging, which diminishes the efficiency of UXO detection system that pass over target sites at high speed (Bell, 2005).

The problem of bridging gaps in the ranging solution due to obstructed or otherwise interrupted signals is solved by integrating GPS (or any other ranging system) with an inertial measurement unit (IMU), which is an autonomous relative positioning device. Indeed, a recently conducted comprehensive program to assess the geolocation technology for UXO detection and remediation (U.S. Army Corps of Engineers, 2006) concluded that all geolocation systems could benefit from augmentation with an IMU. Since IMU's generally also provide very high temporal resolution (50 Hz – 250 Hz), and since GPS is the most efficient and cost-effective ranging tool, the integrated IMU/GPS ranging system is the target of this study for uninterrupted, high-resolution, high-accuracy geolocation in support of UXO detection and characterization.

1.2 Technical Objectives

The three main data processing steps of an integrated IMU/ranging system are data preprocessing, data integration, and post-processing with smoothing. This project focuses on all

three steps, where the first includes de-noising algorithms and self calibration of IMU systematic errors in the field, and the remaining steps are investigated from the viewpoint of optimal filtering and smoothing. The latter include the (extended) Kalman filter, and various nonlinear filters, such as the unscented Kalman filter and particle filter, as well as investigations of the adaptive Kalman filter and the introduction of neural networks to improve the calibration of errors and the overall geolocation solution.

Developing optimal algorithms to integrate the data from ranging systems and inertial measurement units has occupied the navigation community for many years; and, the (Extended) Kalman Filter (EKF) has been the workhorse for IMU/GPS integration for several decades. However, new filters recently introduced and tested have the potential for significant improvements (Aggarwal et al., 2006) over conventional methods that must contend with linear approximations of intrinsically nonlinear dynamics. These new filters, particularly the unscented Kalman filter, are the subject of the present investigation, applied to the precise geolocation of ground-based MEC detector platforms. Since the trajectories of MEC detectors can be highly dynamic with rapid changes in orientation and acceleration, filters that obviate any assumption of linearity should perform better. In addition, particle filters have recently been implemented that avoid the usual assumption of Gaussianity in the sensor errors (Haykin, 2001; Gustafsson et al., 2001; Arulampalam et al., 2001; Simon, 2006). We consider also adaptations of these filters that allow for unknown variations in the sensor and observation noise statistics.

Other studies that have addressed the potential improvement of the unscented Kalman filter over the traditional extended Kalman filter in navigation applications include Van der Merwe and Wan (2004) who predicted up to 30% improvement on an unmanned airborne vehicle (UAV). St. Pierre and Gingras (2004) and Shin (2005) showed only slightly better or mixed results based on simulations for a land vehicle IMU analysis. Yi and Grejner-Brzezinska (2006) also obtained improvement when GPS is blocked (free-inertial navigation), but there was no improvement during periods of GPS coverage.

However, any of these filters cannot overcome the natural accumulation of process errors as the temporal gap in ranging solutions increases, especially in dynamic environments. One method to reduce the divergence between IMU-determined and true trajectories is to apply a post-processing smoothing between GPS updates, such as the Rauch-Tung-Striebel (RTS) backward smoother, which is based on the extended Kalman filter (EKF). We have tailored this type of smoothing to the nonlinear filters (Lee et al. 2008), and for this project the resulting adaptive EKF-RTS smoothing (AEKS) and adaptive UKF-RTS smoothing (AUKS) methods were tested and analyzed using data from an inertial geolocation system. In addition, we tested a simple end-matching algorithm in place of the smoothing, which portends further studies in modeling position errors under in real time that approaches the post-processing precision with known constraints on the dynamics of the vehicle.

We also developed and tested a neural network as an aid to both the adaptive extended Kalman filter/smoother (NN-AEKS) and the adaptive unscented Kalman filter/smoother (NN-AUKS) to bridge outages in the ranging solution for UXO detectors in quiescent and moderately dynamic environments. Finally, we considered the use of dual IMUs in the integrated system with the aim of self-calibrating non-common IMU errors in the post-processing mode using a wave correlation filter (WCF).

2. Technology Description

2.1 The Kalman Filter

The Kalman filter is an optimal (minimum mean square error), linear, recursive estimation method and is amply treated in the literature, as is its extension to deal with non-linear models (Haykin, 2001; Kalman, 1960; Brown and Hwang 1992; Grewal and Andrews 1993). Its application to the IMU/GPS integration problem is also well documented (Greenspan, 1996; Farrell and Barth, 1998; Rogers, 2000; Jekeli, 2000; Titterton and Weston, 2004). The extended Kalman filter (EKF) is founded on two main assumptions: linearity in (or linearization of) the system dynamics and observation models and Gaussian noise excitation (Gordon et al., 1993; Gelb, 1974; Grewal and Andrews 2001). These two factors bring several limitations and implementation difficulties to the integration problem, such as the derivation of the Jacobian matrices for complicated non-linear systems and potentially unrealistic statistical models of the errors (Julier et al., 1995). Also, only relatively small error states are allowed in the EKF, otherwise the first-order approximations can lead to instabilities in the form of biased solutions and inconsistency in the covariance updates.

The basic linear model of a system of error states, x_k, at epoch, t_k, is

$$x_k = F\left(t_k, t_{k-1}\right) x_{k-1} + G_k w_k, \tag{1}$$

$$y_k = H_k x_k + v_k, \tag{2}$$

where F is the state transition matrix; G_k is an appropriate scaling factor for the driving zero-mean Gaussian white noise, w_k; and y_k is an observation linearly related through H_k to the states and also includes zero-mean Gaussian white noise, v_k. The error states typically include position errors, velocity errors, and orientation errors associated with the navigation solution derived from IMU data, and are augmented by various systematic errors assigned to the IMU sensors. The observation (errors) are associated with external navigation aids, such as GPS, which provide information that allows for the estimation of the error states of the system.

The Kalman filter has two steps: first, a prediction of the states at epoch, t_k, given their values at epoch, t_{k-1}; and, second, an update at t_k based on the observation at that epoch. In the prediction, the state estimate and its covariance propagate according to:

$$\hat{x}_k^- = F\left(t_k, t_{k-1}\right) \hat{x}_{k-1}, \tag{3}$$

$$P_k^- = F\left(t_k, t_{k-1}\right) P_{k-1} F^T\left(t_k, t_{k-1}\right) + G_k Q_k G_k^T, \tag{4}$$

where Q_k is the covariance of w_k, P_{k-1} is the covariance matrix of the states at the epoch, t_{k-1}. Updating the states on account of the observations yields

$$\hat{x}_k = \hat{x}_k^- + K_k\left(y_k - H_k \hat{x}_k^-\right), \tag{5}$$

$$P_k = \left(I - K_k H_k\right) P_k^- \left(I - K_k H_k\right)^T + K_k R_k K_k^T \tag{6}$$

where R_k is the covariance of the observation noise and the Kalman gain is given by

$$K_k = P_k^- H_k^T \left(H_k P_k^- H_k^T + R_k\right)^{-1} \tag{7}$$

For later use, we also define the innovation and its estimate, as in equation (5),

$$u_k = y_k - H_k x_k^- \tag{8}$$

$$\hat{u}_k = y_k - H_k \hat{x}_k^- . \tag{9}$$

2.2. Sampling-Based Filters

The sampling-based filtering methods differ from the standard Kalman filter in that they propagate sample states rather than their statistics through the system model. As such, no linearization is required, nor is it required to formulate and compute the attendant derivatives of the system model. Depending on the statistical assumptions for the states, the propagated samples are analyzed to infer the propagated statistics. We consider two sampling-based filters, the unscented Kalman filter (UKF, also called sigma-point Kalman filter) and the particle filter (PF). The UKF avoids the linearization associated with the EKF, but still assumes Gaussian state variables, and the estimation of the propagated statistics is achieved on the basis of the unscented transformation (Wan and Van Der Merwe, 2001). The PF obviates both the linearization and the Gaussianity assumption by propagating a sufficient number of samples based on the Monte Carlo approach to statistics estimation.

2.2.1 Unscented Kalman Filter (UKF)

The development of the unscented Kalman Filter was initiated by Julier and Uhlmann (1996) and Julier et al. (1995; 2000). The UKF is a recursive application of the unscented transformation (UT) of state variables through the nonlinear state dynamic model. The UT propagates a suitably chosen set of sample points (called sigma points) in the state space through the (nonlinear) system dynamics such that they accurately capture the transformed mean and covariance of the states. We use the more general scaled version of the UT given by Wan and Van der Merwe (2001). For the random variable x (dimension, n_x) with mean, $\bar{x}$, and covariance, P_x, the $2n_x + 1$ sigma points are generated as follows

$$\begin{aligned} c_0 &= \bar{x} \\ c_i &= \bar{x} + a\left(\sqrt{\left(n_x + k\right) P_x}\right)_i, \quad i = 1, \ldots, n_x \\ c_i &= \bar{x} - a\left(\sqrt{\left(n_x + k\right) P_x}\right)_i, \quad i = n_x + 1, \ldots, 2n_x \end{aligned} \tag{10}$$

where a and k are scaling parameters and $\left(\sqrt{(n_x+k)P_x}\right)_i$ is the ith row or column of the matrix square root of $(n_x+k)P_x$. Given a nonlinear function, $g(x)$, it can be shown that the following weighted combinations of $y_i = g(c_i)$ estimate the first two statistical moments (mean and covariance) of g at least up to second order in the non-linearities:

$$\bar{y} = \sum_{i=0}^{2n_x} W_i^{(m)} y_i, \quad P_y = \sum_{i=0}^{2n_x} W_i^{(c)} (y_i - \bar{y})(y_i - \bar{y})^T, \tag{11}$$

where the corresponding weights are given by

$$\begin{aligned} W_0^{(m)} &= 1 - \frac{n_x}{a^2(n_x+k)}, \quad W_0^{(c)} = 1 - \frac{n_x}{a^2(n_x+k)} + \left(1 - a^2 + b\right) \\ W_i^{(m)} &= W_i^{(c)} = \frac{1}{2a^2(n_x+k)}, \quad i = 1, \ldots, 2n_x \end{aligned} \tag{12}$$

The sum of the weights for the mean is unity, while for the covariance they sum to $\left(1 - a^2 + b\right)$. The scaling parameter, a ($10^{-4} \le a \le 1$), controls the spread of the sigma points around $\bar{x}$ and serves to maintain the positive semi-definiteness of the covariance (Wan and Van Der Merwe, 2001). For Gaussian states, x, the estimation of the mean and covariance of g is accurate up to third order. The scaling parameter, b, in addition to a, is used to increase the accuracy of higher-order moments (for Gaussian variables, $b = 2$ is optimal). The scaling parameter, k, was set to $k = n_x$ in our simulations, and we varied a.

The linear propagation and observation of states defined by equations (1) and (2) are replaced by the more general non-linear forms; however, we still assume additive noise:

$$x_k = f(x_{k-1}) + G_k w_k, \tag{13}$$

$$y_k = h(x_k) + v_k. \tag{14}$$

The Kalman filter using the unscented transformation, i.e., the UKF, then proceeds with the usual two-step, prediction and filter formalism, but the mean and covariance are determined from the sigma points.

2.2.2 Unscented Particle Filter (UPF)

The particle filter was introduced already in the 1950s, but was forgotten due to the lack of computing power (Godsill et al., 2000). However, with modern computational capabilities, the particle filter has also been applied to INS/ranging-system integration (Angermann et al., 2006) and to the problem of transfer alignment (Hao et al., 2006). The performance of the PF generally

improves as the number of sample states (particles) used to capture their probability density function (pdf) increases, which, however, also increases the computational burden. There are three types of particle filter, the generic (or traditional) particle filter, the unscented particle filter (UPF, also called sigma-point particle filter), and the extended particle filter. We considered only the UPF.

Particle filters, also known as bootstrap filtering, the condensation algorithm, Monte Carlo filtering, and survival of the fittest methods, implement Bayesian estimation, which under the special case of Gaussian noise and linear models yields the familiar Kalman filter (Gordon et al., 1993). The object is to determine the probability density of the state at time, t_k, conditioned on the measurements up to that time, according to Bayes' Rule (Simon, 2006, p.464)

$$p\left(x_k \mid y_k, y_{k-1}, y_{k-2}, \ldots\right) = \frac{p\left(y_k \mid x_k\right) p\left(x_k \mid y_{k-1}, y_{k-2}, \ldots\right)}{p\left(y_k \mid y_{k-1}, y_{k-2}, \ldots\right)}, \tag{15}$$

where the conditional density, $p\left(y_k \mid x_k\right)$, is presumed known (for example, but not necessarily Gaussian), and the other conditional densities on the right side, in principle, can be determined from the previous steps in the recursive algorithm.

In practice, the particle filter starts with the randomly generated particles, $x_{0,i}$ $, i = 1, \ldots, N$, using their a priori mean and covariance and propagates them through equation (13):

$$x_{k,i} = f\left(x_{k-1,i}\right) + G_k w_{k,i}, \tag{16}$$

where $w_{k,i}$ is the noise realized according to its known pdf. From the measurement, y_k, and its known pdf, the likelihood, $q_i = p(y_k / x_{k-1,i})$, can be computed for each particle. These relative likelihood values, normalized to sum to unity, are then used to obtain a re-sampling of the particles, whose pdf (now conditioned on the observations) tends to the desired Bayesian density (equation (15)). From this the mean and covariance can be computed in the usual ways. There are several re-sampling techniques and particle modifications available to improve the performance of the filter. We used the sequential importance sampling (SIS)) method (Haykin, 2001; Wan and Van Der Merwe 2001).

Van der Merwe et al. (2000) combined the PF with other filters such as UKF in order to refine the initially generated particles, and called it the unscented particle filter (UPF). Each randomly generated initial particle is propagated and updated by using the UKF (where the sigma points are computed using the particle). Then, the likelihood values are determined using these a posteriori particles and the measurement pdf, as before, followed by the re-sampling procedure (Haykin, 2001; Simon, 2006). This approach can yield a better approximation for the conditional pdf of the states and has yielded improved accuracy for various positioning-related applications (Arulampalam et al., 2001; Grewal and Andrews, 2001; Van der Merwe et al., 2000).

2.2.3 Rao-Blackwellized Unscented Particle Filter (RBUPF)

To overcome the computational inefficiency of the PF, the states can be divided into two subsets (linear and non-linear) and this type of filter is called the Rao-Blackwellized particle filter (RBPF) (Nordlund and Gustafsson, 2001). The RBPF applies the Kalman Filter to the linear and Gaussian states of the system model. The remaining state variables, which suffer from severe non-linear and/or non-Gaussian structure, are solved using the unscented particle filter.

Partitioning the state vector x_k into non-linear, x_k^1, and linear, x_k^2, parts the system and measurement models become (compare equations (1) and (2) for the linear case and equations (13) and (14) for the general non-linear case):

$$\begin{aligned} x_{k+1}^1 &= f^1\left(x_k^1\right) + F_k^1 x_k^2 + w_{k+1}^1 \\ x_{k+1}^2 &= f^2\left(x_k^1\right) + F_k^2 x_k^2 + w_{k+1}^2 \\ y_k &= h\left(x_k^1\right) + H_k \cdot x_k^2 + v_k \end{aligned} \tag{17}$$

The system noise vector is divided into two noise vectors, w_k^1 and w_k^2 that are uncorrelated, and have known covariance matrices, $Q_k^1 = E\left(w_k^1\left(w_k^1\right)^T\right)$ and $Q_k^2 = E\left(w_k^2\left(w_k^2\right)^T\right)$, respectively. To compute the a posteriori pdf of the filter, we estimate $p\left(x_k \mid y_k\right) = p\left(x_k^1, x_k^2 \mid y_k\right)$ by factoring it into two parts according to Doucet et al. (2001) and Nordlund (2002),

$$p\left(x_k^1, x_k^2 \mid y_k\right) = p\left(x_k^2 \mid x_k^1, y_k\right) p\left(x_k^1 \mid y_k\right), \tag{18}$$

and by first computing each pdf on the right side according to the appropriate filter methods.

2.3 Adaptive Filtering

The drawback of the navigation filters discussed so far is that they are adversely affected by potentially inaccurate system and measurement noise statistics. Particularly for highly dynamic trajectories (such as may be encountered by UXO detection equipment) the error statistics may vary in time, thus invalidating the initially defined models. To improve the filters under such circumstances and mitigate such effects, adaptive methods are often employed.

Among the various parameters that require a priori specification in the UKF, including the initial states and their covariance, the unscented transformation parameters, and the covariances of the process noise (Q) and measurement noise (R), the latter influence most significantly the filter's performance and stability. The initial states and covariance have negligible influence as the filter processes more and more data. The UT parameters only affect the higher order terms of the nonlinear model and have little impact on the accuracy of the estimated position (Lee and Jekeli, 2009). Therefore, usually an innovation based covariance matching algorithm is employed in order to tune the Q and R matrices of the Kalman filter.

This technique is based on the supposition that the actual filter residuals should be consistent with their theoretical covariance (Jwo and Huang, 2004). In this paper, since a loosely-coupled INS/GPS system was employed, we considered only the system (IMU) noise. According to

Salychev (1999), the a priori information of the system (as represented by the covariance matrices, Q) can be adjusted according to the accuracy of estimation.

If covariance matrix, R_k, is unknown or inaccurate, it can be estimated from the covariance matrix of the innovation sequence ($\hat{u}_k$, equation (9)). From equation (8), with $P_k^- = E\left(x_k^-\left(x_k^-\right)^T\right)$, let

$$C_k = E\left(u_k u_k^T\right) = HP_k^- H^T + R_k , \tag{19}$$

Then, let an estimate of this covariance be

$$\hat{C}_k = \frac{1}{m}\sum_{j=k-m+1}^{k} \hat{u}_j \hat{u}_j^T , \tag{20}$$

where m is the estimation window size, which satisfies the recursion:

$$\hat{C}_k = \frac{k-1}{k}\hat{C}_{k-1} + \frac{1}{k}\hat{u}_k \hat{u}_k^T . \tag{21}$$

Substituted into equation (19), it yields an estimate of the measurement covariance matrix:

$$\hat{R}_k = \hat{C}_k - HP_k^- H^T . \tag{22}$$

In case the covariance of the system noise, Q_k, is unknown, it can be shown similarly that

$$GQ_k G^T = K_k E\left(u_k u_k^T\right) K_k^T , \tag{23}$$

from which we approximate

$$G_k \hat{Q}_k G_k^T = K_k \hat{C}_k K_k^T . \tag{24}$$

Originally developed for the KF (and EKF) this technique has also been employed for the UKF (Song and Han 2008). We have also applied this technique to the particle filter and call it the Adaptive Unscented Particle Filter (AUPF). It is implemented and validated by the tests of the simulations described in Section 3.

2.3.1 Neural Network Aided Adaptive Filtering

The adaptive estimation of the covariance using equation (20) depends on the proper choice of the window size, which for optimal results may be variable and difficult to determine (Jwo and Huang, 2004). Because of this potential shortcoming, we considered modifying these adaptive filters using methods applied in artificial intelligence (AI). AI provides a successful and

effective solution to certain engineering and science problems which cannot be solved by using conventional methods (Cawsey, 1998). Various approaches such as neural networks, fuzzy logic, evolutionary computing, probabilistic computing, expert program, and genetic programming can provide an "artificial intelligence" (defined as the ability to learn, understand and adapt) to complex and uncertain systems (Honavar and Uhr, 1994). Among these techniques, we selected the neural network to aid adaptive filters because it can learn input-output relationships without a priori knowledge of the dynamic models and noise statistics of the measurements. Employing the neural network for similar applications has already been demonstrated with success by Jwo and Huang (2004), Wang et al. (2006, 2007), Korniyenko et al. (2005), and Chiang and El-Sheimy (2004). Specifically, Wang et al. (2006) proposed a neural network and Kalman filter hybrid approach to reduce KF drift during GPS outages. Also, Wang et al. (2007) used the neural-network-aided adaptive KF to reduce vehicle dynamic variations and to improve the navigation solution. And, Zhan and Wan (2006) derived a multi-layer, neural-network-based unscented Kalman filter for nonlinear estimation, and their simulation results showed overall improvement of the filter performance.

A neural network consists of neurons that process an input to generate an output (Figure 1). The neuron includes a synaptic weight (or weight), an adder, and a transfer (activation) function (Haykin, 1999). An input signal, x_i ($i = 1,2,\ldots,n$), is multiplied by a synaptic weight, w_{ji}, and connected to neuron, j. An adder sums up the weighted input signals (simply, $v_j = \sum_{i=1}^{n} w_{ji} x_i$). The neuron model also has a bias, b_j (also called the external threshold) that is used to increase or decrease the input to the transfer function. Therefore, the simple model of a neuron is

$$y_j = f\left(\sum_{i=1}^{n} w_{ji} x_i - b_j\right), \tag{25}$$

where f is a transfer function and y_j represent the output.

A transfer function modifies and limits the amplitude range of the output signal, typically normalizing it in the range of [0,1] or [-1,1]. Common transfer functions, selected according to the application, include the hard limiter (a binary or bipolar output), a linear (or piecewise linear) function, and the sigmoid (s-shaped) nonlinear function (Haykin, 1999). We use the sigmoid function, $f(v) = \left(1 + e^{-av}\right)^{-1}$, with slope parameter, a, because the relationship between input and output in our case is essentially non-linear (see also Ham and Kostanic, 2001).

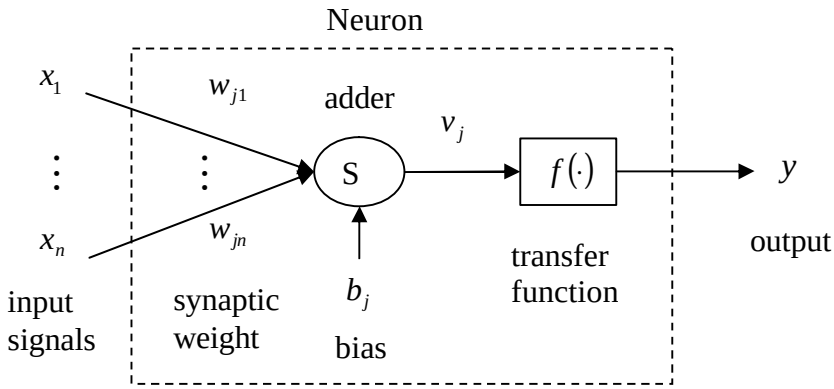

Figure 1: The neuron with three basic elements.

The neurons are used to form layers that build a neural network. The architecture of the network can be classified as single-layer feed-forward (one hidden layer and an output layer; SFN), as multi-layer feed-forward (multiple hidden layers and an output layer; MFN), and as recurrent (at least one feedback loop based on a SFN or a MFN; RN) (Haykin, 1999). Demuth and Beale (2004) showed that the two-layer feed-forward network (first layer is sigmoid and second is linear) can be trained to approximate any arbitrary nonlinear function. Golden (1996) also showed that an MFN can be designed to provide the best approximation accuracy to the unknown model. We applied the multi-layered feed-forward neural network (three layers) to aid the various adaptive filtering techniques for the INS/GPS system.

The usual way to decide on the appropriate number of hidden neurons is empirical (however, see also Bishop, 1995; and Haykin, 1999). That is, many candidate networks having different numbers of hidden neurons should be tested to determine the one with the best performance. Our laboratory tests indicate that optimal geolocation results are obtained with 16, 24, and 15 neurons, respectively, in the three layers, where sigmoid transfer functions are used in the first and second layers and the third layer is linear.

The principal idea for this project is the hybrid method of traditional adaptive covariance estimation aided by a neural network trained on given platform dynamics. The Kalman filter estimates the navigation errors in position, velocity and attitude using external control. At the same time, the neural network is trained to map a relationship between the platform dynamics (the input) and the Kalman filter estimations (the desired output). The input comprises changes in velocity ($\Delta v_N, \Delta v_E, \Delta v_D$) in a local north-east-down coordinate frame, and Euler angles, f, q, y, for the platform attitude, and their changes, $\Delta f, \Delta q, \Delta y$. The Euler angles are determined from the gyro data and the changes in these and in the velocity are calculated from the *last* measurement update to the *current* measurement update:

$$\Delta v_N = v_{N,k+1} - v_{N,k}, \quad \Delta v_E = v_{E,k+1} - v_{E,k}, \quad \Delta v_N = v_{D,k+1} - v_{D,k}$$
$$\Delta f = f_{k+1} - f_k, \quad \Delta q = q_{k+1} - q_k, \quad \Delta y = y_{k+1} - y_k \tag{26}$$

where k is the measurement update index.

Wang et al. (2006, 2007) suggested that rapid changes in the heading angle can disturb the training of the neural network. However, in our laboratory tests, training with the heading angle produced better results because this angle clearly identifies the dynamic maneuvering of the platform. For the neural network's desired outputs (d), we selected the innovations of the Kalman filter, given by equation (9). For the unscented Kalman filter the desired output of the neural network is $y_k - \bar{y}_k$ ($\bar{y}_k$ is from equation (11)).

If measurements (external control points) are available, the neural network is trained at the control update rate using all available input and desired output values until it reaches a certain pre-defined error (threshold). The weights and biases of the network were adjusted iteratively using the Levenberg-Marquardt algorithm to minimize the differences between the *computed* output, *y*, and the *desired* output, *d* (Chiang and El-Sheimy, 2004; Wang et al., 2006). When measurements are not available (during a GPS outage), the computed output of the neural network is used to determine the process noise covariance (GQG^{T}) according to equations (24) and (20). In our Laboratory tests, since the neural network does not have enough training data from the first few control points, the process noise (Q) is estimated by the traditional adaptive filtering method (equation (24)) until the neural network is successfully trained.

2.4 Smoothing

The filters described above are recursive algorithms based on the conditional expectation of the state given all observations and states up to the current time step *k*. In contrast, smoothing estimates the states by using also available observations in the future.

2.4.1 Kalman Smoother (KS)

From given observations over the interval $0 < k \le N$ for fixed N, if the forward and backward estimate ($\hat{x}_k^f$ and $\hat{x}_k^b$) and their error covariances (P_k^f and P_k^b) are available, the smoothed estimate, $\hat{x}_k^s$, and its covariance, P_k^s, are obtained. Since it is assumed that the process noise w_k and measurement noise v_k are independent, we may formulate the smoothed estimate and its a posteriori error covariance matrix as

$$\begin{aligned} \hat{x}_k^s &= P_k^s \left(\left[P_k^f \right]^{-1} \hat{x}_k^f + \left[P_k^b \right]^{-1} \hat{x}_k^b \right) \\ P_k^s &= \left[\left[P_k^f \right]^{-1} + \left[P_k^b \right]^{-1} \right]^{-1} \end{aligned} \tag{27}$$

This smoother (three-part smoother) has three components; a forward filter, a backward filter, and a separate smoother which combines results embodied in the forward and backward filters (Haykin, 2001). However, The Rauch-Tung-Striebel (RTS) smoother differs from this smoother in that the measurements are processed by the forward filter and then a separate backward smoothing pass is used to obtain the smoothing solution (Sarkka, 2008). Also, the Rauch-Tung-Striebel smoother is more efficient than the three-part smoother in that a single entity can perform smoothing by incorporating the backward filter and separate smoother (Rauch et al., 1965).

2.4.2 Particle Filter Smoothing

In a literature review on particle smoothing or Monte Carlo Smoothing, it is (interestingly) noticed that although particle filter theory and applications are frequently treated, there are only few published papers on particle filter smoothing because the smoothing algorithms such as the two-filter smoother (TFS), the forward-backward smoother (FBS), and a maximum a posteriori (MAP) smoother typically incur high computational costs, namely of the order of $O(N^2)$, compared to the PF which has costs of the order of $O(N)$ (Klass et al., 2006).

The basic idea of particle smoothing is that the particle filter can provide a smoothed result automatically if the whole history of each particle of states is stored (Kitagawa, 1996). That is, from the filtered particles of the UPF, each particle is smoothed by using the unscented RTS (Sarkka, 2006). Each smoothed particle can be defined as $\hat{x}_k^{s(i)}$, $i = 1, \ldots, N$ (N is the number of particles) and then the mean value of the smoothed estimate can be found from a simple average (Kitagawa, 1996; Sarkka, 2008):

$$\hat{x}_{k\,mean}^{s} \approx \frac{1}{N} \sum_{i=1}^{N} \hat{x}_k^{s(i)} \,. \tag{28}$$

2.4.3 Rao-Blackwellized Particle Smoother (RBPS)

For the smoothing version of the RBPF we can employ the same method as for the UPS, which employed the unscented RTS algorithm to smooth each particle. The RTS smoother was applied to each of the mean and covariance histories of the particles, $\hat{x}_{1:N}^{(i)}$, $P_{1:N}^{(i)}$, $i = 1, \ldots, N$ to produce the smoothed mean and covariance $\hat{x}_{1:N}^{S}$, $P_{1:N}^{S}$.

2.5 Wave Correlation Filter

The Wave Correlation filter (WCF) ideally extracts common spectral components from two signals, while rejecting disparate ones, thus removing errors if the two signals are supposed to refer to the same source. Of course, common errors are not removed. With this filter we anticipate obtaining a more accurate positioning solution from the dual IMU measurements, where random errors left in the two final solutions should be uncorrelated and amenable to elimination or reduction by the WCF (a similar approach was used, e.g., by Serpas (2003) and by Li (2009) to improve solutions derived from independent data sets). Let the two EKF solutions along the trajectory be denoted $\hat{x}_1(k)$ and $\hat{x}_2(k)$, respectively. The corresponding Fourier transforms are $G_1(l)$ and $G_2(l)$, where l is the wave number. The correlation coefficient, r_l, per wave number is obtained by

$$r_l = \frac{\mathrm{Re}\big(G_1(l)\big)\mathrm{Re}\big(G_2(l)\big) + \mathrm{Im}\big(G_1(l)\big)\mathrm{Im}\big(G_2(l)\big)}{\big|G_1(l)\big|\big|G_2(l)\big|} \tag{29}$$

Each solution is filtered according to a pre-defined threshold:

$$\bar{G}_{1,2}(l) = \begin{cases} G_{1,2}(l) & if \;\; r_l \geq threshold \\ 0 & if \;\; r_l < threshold \end{cases} \tag{30}$$

The final position estimates are obtained by transforming the average of the retained frequency components back into the time domain:

$$\hat{p}(k) = \frac{1}{2} F^{-1}\left\{\bar{G}_1(l) + \bar{G}_2(l)\right\}, \tag{31}$$

where is F the Fourier transform.

2.6 End-Matching

The remaining trend and bias errors of both the EKF and UKF solutions after WCF processing could be corrected in an ad hoc manner by the end-matching method with respect to the GPS positions. In terms of latitude, longitude and height coordinates, the end-matching algorithm is a simple linear fit to given data at the ends of a free-inertial trajectory:

$$\underbrace{\begin{bmatrix} \tilde{f}_r \\ \tilde{l}_r \\ \tilde{h}_r \end{bmatrix} - \begin{bmatrix} \hat{f}_w \\ \tilde{l}_w \\ \hat{h}_w \end{bmatrix}}_{Y} = \underbrace{\begin{bmatrix} 1 & (t-t_0) \\ 1 & (t-t_0) \\ 1 & (t-t_0) \end{bmatrix}}_{A} \underbrace{\begin{bmatrix} b_0 \\ m \end{bmatrix}}_{X}, \tag{32}$$

where $\tilde{f}_r, \tilde{l}_r, \tilde{h}_r$ are GPS points, $\hat{f}_w, \hat{l}_w, \hat{h}_w$ are the position after filtering with wave correlation filter. b_0 is a bias and m is the trend as a function of epoch. The values of bias and trend (matrix X) can be found by

$$\hat{X} = \left(A^T A\right)^{-1} \cdot A^T Y . \tag{33}$$

3. Filter Simulations

The initial investigations were based on simulations to ascertain the general performance of the different filters and smoothers under typical MEC survey geometries and dynamics. Without loss in generality, we selected the loosely coupled INS/GPS integration scheme based on the decentralized filter architecture (Jekeli, 2000). A tightly integrated system typically would be used in GPS embedded inertial navigation systems, where both the IMUs and the GPS aid each other to obtain an optimal blended solution. Looking toward our eventual applications where an isolated IMU would be added to an existing geolocation system, the loosely coupled integration seemed more appropriate.

3.1 Simulation Setup

Aside from the different filtering methods, a number of system and environmental factors were considered, including the IMU sensor quality, the dynamics of the detector platform (typical for either hand-held or cart-mounted deployment), and the ranging solution quality (concerning both precision and environmental degradation, as well as longer outages). The IMU sensor may be categorized as commercial grade (e.g., Crossbow IMU400C), tactical or medium grade (e.g., Honeywell HG1700), and navigation grade (e.g., Litton/Northrop-Grumman LN100). Table 1 offers representative specifications, as published by the corresponding vendors, for the most important errors associated with the accelerometers and gyroscopes for each grade of inertial unit.

Table 1. IMU levels of accuracy.

IMU	Accelerometer			Gyroscope		
	Bias	Scale	Random walk	Bias	Scale	Random walk
IMU400C	8.5 mg	10^4 ppm	5 mg/$\sqrt{hr}$	3600 °/hr	10^4 ppm	0.85 °/$\sqrt{hr}$
HG1700	1.0 mg	300 ppm	0.25 mg /$\sqrt{hr}$	1 °/hr	150 ppm	0.125 °/$\sqrt{hr}$
LN-100	20 µg	40 ppm	5.0 µg/$\sqrt{hr}$	0.01 °/h	1 ppm	0.001 °/$\sqrt{hr}$

The two levels of ranging precision are associated with either radar or laser ranging, exemplified by real-time kinematic (RTK), geodetic quality, differential GPS (e.g., Trimble 4700 receiver) and the geodetic total station (e.g., Leica TPS1100 total station). Each level of precision is affected by the distance, respectively, to the fixed GPS base station and to the total station (Clynch, 2001; Grejner-Brzezinska, 2001; Kim, 2004). Table 2 lists typical precision levels considered in our analysis. Further degradation in the ranging solution will occur primarily because of signal occlusions (although other factors, such as tropospheric and ionospheric delays, and the geometric configuration of the transmitters, also affect the signal and solution quality). Signal outages may occur because of intervening manmade structures or natural objects (usually a foliage canopy in the case of GPS; also rugged terrain in case of the total station). We assume relatively short-lived outages on the order of several to tens of seconds. It should be emphasized that while our analyses address primarily the inertial sensor

capability to aid the ranging solution in an operational setting, for this investigation the ranging solution is also viewed as the means to estimate inertial sensor errors.

Table 2. The assumed precision of ranging solutions.

	Performance (s_r)
RTK-DGPS	Horizontal: 10mm + 1ppm Vertical: 20mm + 1ppm
Total Station	Horizontal & Vertical: 2mm + 2ppm

Four different filtering algorithms were implemented and compared in our simulations: the extended Kalman filter (EKF), the unscented Kalman filter (UKF), the unscented particle filter (UPF), and the adaptive unscented particle filter (AUPF). In order to assess these filters in typical dynamic environments for MEC detection and characterization, the accuracy of the integrated positioning system was determined separately for curved and straight sections of the trajectory. We also considered tuning the parameters of the unscented transformation, and evaluated the benefits of using the particle filters when the input noise is non-Gaussian.

The state vector for the IMU/ranging integrated solution comprises 21 states: three position (latitude, longitude, height) errors, (df, dl, dh); three velocity errors, ($d\dot{f}, d\dot{l}, d\dot{h}$); three orientation errors in a local north-east-down frame, (y_N, y_E, y_D); and a bias and scale factor error for each of the three accelerometers and three gyros. For the UKF and UPF, instead of the three orientation angle errors, the four corresponding quaternions were employed because the UT operates best in a Euclidean space (i.e., this avoids the transcendental functions) (Shin, 2005; Kraft, 2003).

For a given trajectory, error-free IMU data were generated using the Matlab INSToolkit®. The input and output specifications of INSToolkit are described in (Jekeli and Lee, 2007). The trajectory was defined for a platform following a planar path with 0.5 m/s velocity and meandering sweeps across a given area. The generated accelerometer data are velocity increments, Dv, and the gyro data are angle increments, Dq. The temporal resolution of this control trajectory was $0.02\ \mathrm{s}$.

The actual error-corrupted IMU data were then simulated using errors specified in Table 1 according to the models

$$\begin{aligned} D\tilde{q} &= (1+k_G)Dq + (d+w_G)Dt \\ D\tilde{v} &= (1+k_A)Dv + (b+w_A)Dt \end{aligned} \tag{34}$$

where d, k_G, and w_G are the bias, scale factor error, and random noise for the gyro; and b, k_A, and w_A, are corresponding quantities for the accelerometer. The time interval between the generated data is $Dt = t_{k+1} - t_k$ (0.02 s in our simulations). Corresponding navigation equations for the IMUs were integrated using these corrupted data to generate the trajectory coordinates as indicated by an inertial navigation system.

In addition, the ranging solution for the trajectory was determined by simply adding random noise to the true coordinates. That is, we assumed the ranging system to be free of all systematic errors and the final solution corrupted only by white noise:

$$\begin{aligned} \tilde{f}_r &= f_r + n \cdot s_r \\ \tilde{l}_r &= l_r + n \cdot s_r \\ \tilde{h}_r &= h_r + n \cdot s_r \end{aligned} \tag{35}$$

where n is a random variable following the zero-mean, unit-variance Gaussian distribution, and s_r is given in Table 2. The ranging solution coordinates are used in the filter to update the IMU position errors and to estimate the systematic errors in the inertial sensors. The Figure 2 shows the simulated trajectory, designed for typical MEC mapping and detection, with 18 180° turns and 19 straight segments. The turns represent highly non-linear dynamics as modeled by the navigation equations and generally pose a challenge to linearized filters such as the EKF. The ranging updates in the filter can be introduced at longer intervals to simulate prolonged interruptions. Figure 3 shows the general simulation and analysis process.

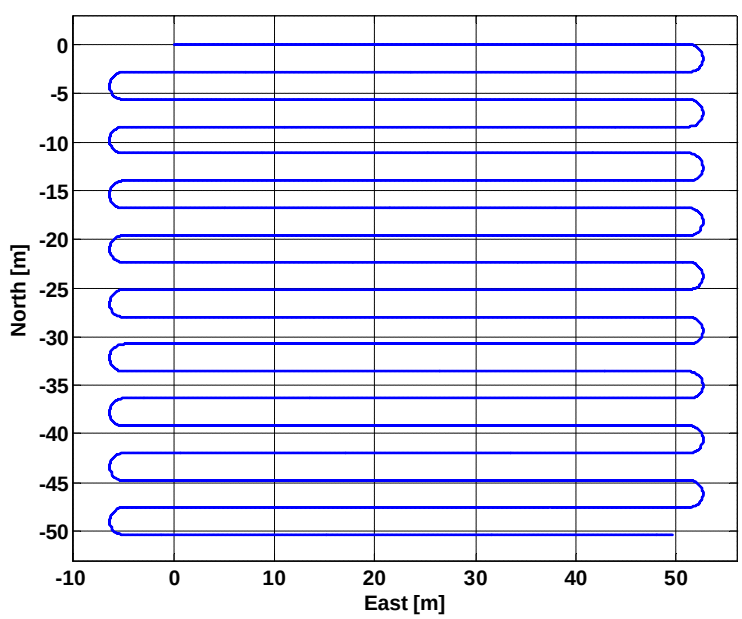

Figure. 2. The generated control path.

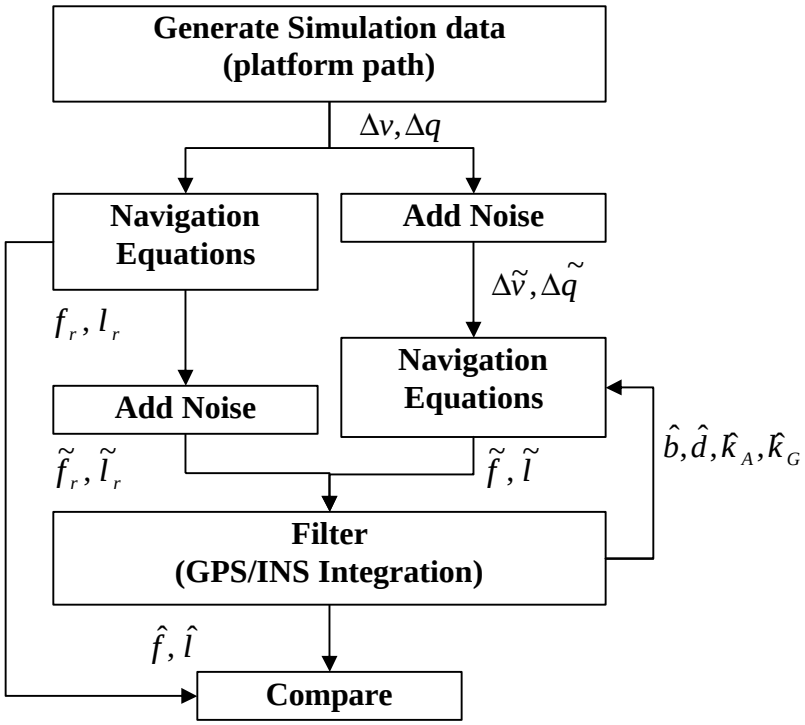

Figure 3. Flow chart of loosely coupled, decentralized ranging/IMU integration and simulation analysis.

3.2 Results and Analysis

The free-inertial navigation solutions obtained just prior to incorporation of the external updates using the EKF, UKF, and UPF, at intervals of 1 s, 10 s, and 30 s were compared with the control trajectory. The ranging solution updates are either GPS or total station observations and all three categories of inertial sensors were tested. Within each set of sensor/update tests, the position errors are a function of how well the filter estimates the systematic errors of the inertial sensor in the particular non-linear environment.

The comparison against the control was based on the total-distance errors, computed from the three coordinate errors; and, their standard deviations for each of the curved and straight sections of the test trajectory (Figure 2) were averaged. Figure 4 (for 1 s updates only) shows that, as expected, the more precise updates (total station vs. GPS) yield more accurate free-inertial solutions simply because the integration of the inertial sensor outputs begins with a smaller error. Interestingly, for this particular simulation, there is little difference between the high-end and the medium quality inertial sensors showing that either one will offer similar interpolation capability within 1 second. Clearly, the EKF does not perform as well as the UT-based filters, particularly along the curved segments of the trajectory. The UPF offers only slightly better performance than the UKF in these tests because the simulated noise processes for the inertial sensors and the observation updates are Gaussian. As the interval before the next update increases, the inertial sensor errors accumulate in the position solution, but the UKF and UPF still out-perform the EKF, as shown in Figure 5 for just GPS and the medium-grade IMU. We note that the position accuracy of the filters (no additional smoothing) is useful only for screening of MEC if the GPS outage reaches 10 s.

Besides outright interruptions in the ranging solution, it may also be degraded during several seconds of the survey. We consider only differential GPS solutions and assume that such degradation is a function of baseline length between the rover and the fixed base station. Using the corresponding increased observation noise, as shown in Table 2, Figure 6 compares the EKF and UKF performances with respect to the medium-grade IMU, free-inertial, positioning accuracy at the end of 1 s and 5 s prior to degraded GPS updates. Again, we find improved results for the UKF over the EKF, especially, when both the degradation and the update interval increase.

The superiority of the UKF may be realized only with appropriate tuning of the scaling parameter, a (since the error states are excited by Gaussian noise, the optimal value $b = 2$ was used for these tests). The results of Figure 4 and 5 were obtained with $a = 0.15$, corresponding to sigma points within a range of $\pm 1s$. Expanding this range did not improve the estimation, but significantly smaller values of a degrade the performance of the UKF, as also shown in Figure 6, which includes results for $a = 0.0005$, $a = 0.001$, and $a = 0.01$.

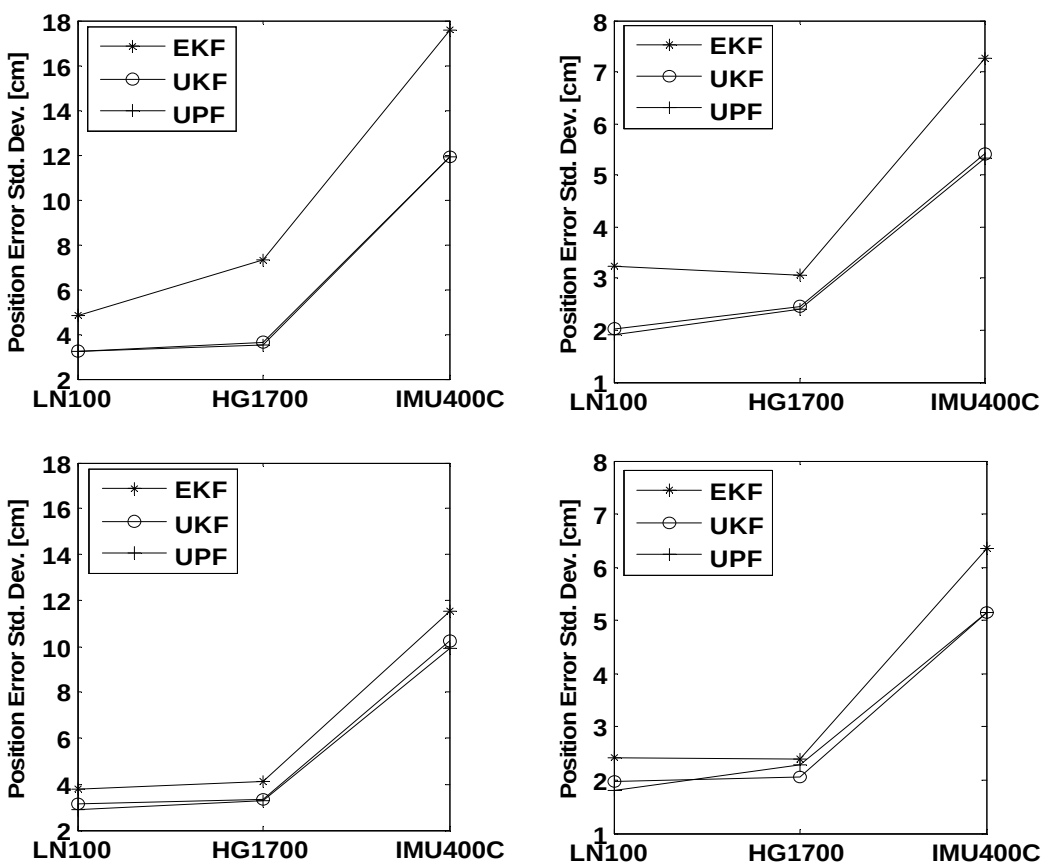

Figure 4: Standard deviation of errors of different IMU grades with 1 s ranging system updates using different filters (first row: curve segments, second row: straight segments, first column: GPS, second column: total station) (units: cm).

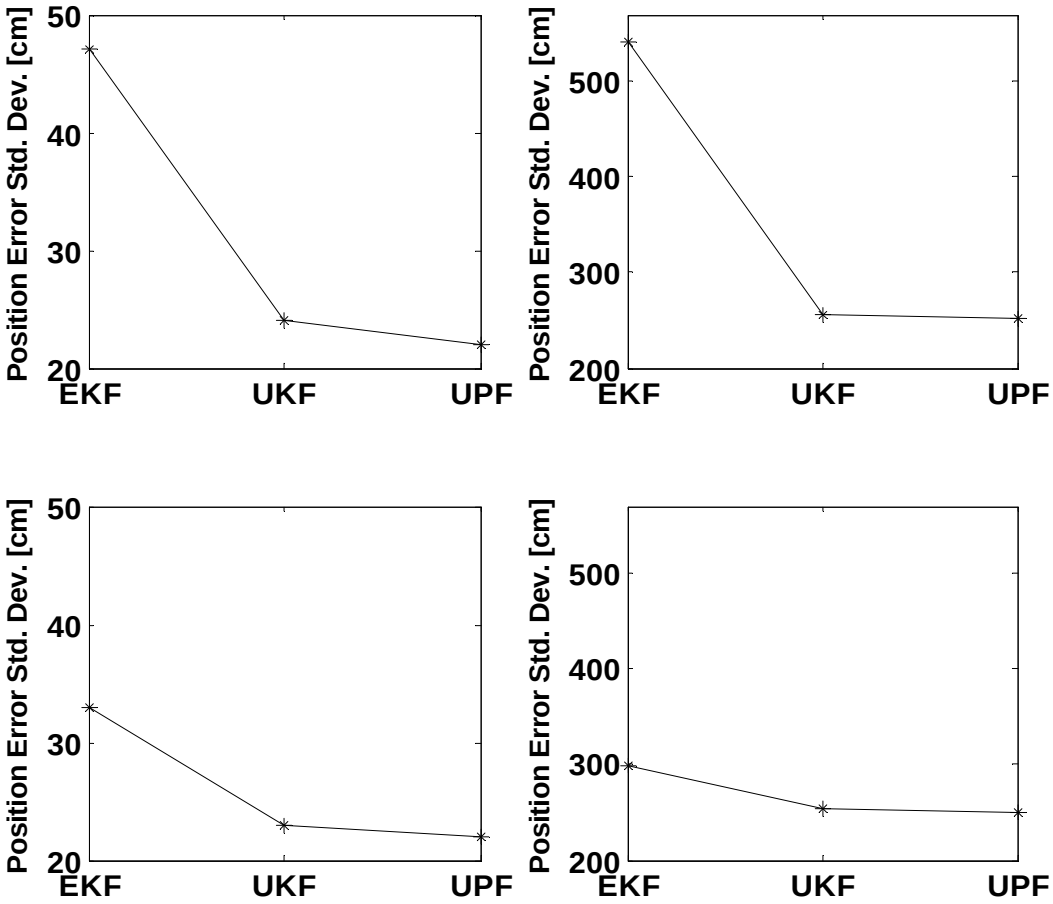

Figure 5: Standard deviation of errors for different filtering methods (first row: curve segments, second row: straight segments, first column: 10 s, second column: 30 s GPS updates of the medium-grade IMU) (units: cm).

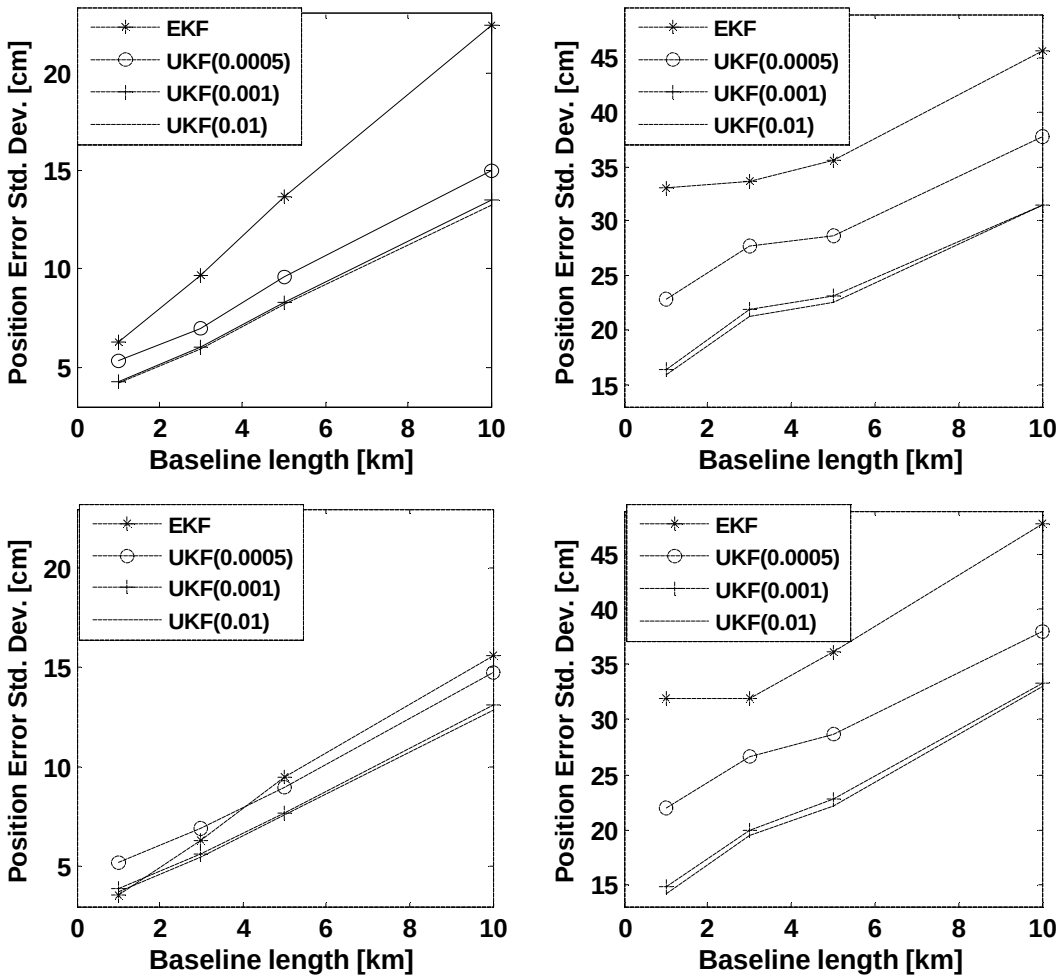

Figure 6: Standard deviation of errors with medium-grade IMU and degraded GPS updates and with different scales in the unscented transformation (first row: curve segments, second row: straight segments, first column: GPS 1 s updates, second column: GPS 5 s updates).

The foregoing tests assumed a system driven by Gaussian noise. We may expect similar results with other symmetrically distributed processes, and the UKF could also be tuned to deal with non-Gaussian, symmetric distributions using the parameter, b . On the other hand, dynamic systems, besides being generally non-linear, may also be excited by *non-symmetric* processes (Kushner, 1967). Indeed, Reddy and Herr (2006) investigated the skewness of IMU sensor errors. Julier (1998) and Naveau (2005) also proposed modeling the process noise with asymmetric probability densities. We considered both symmetric non-Gaussian as well as asymmetric distributions to determine the performance of the particle filter. In one test, sensor errors were generated from a uniform distribution with the same variance as in the Gaussian case. As seen in Table 3, the latitude and longitude standard deviations are slightly lower in value with the particle filter. There is very little or no difference with respect to the Gaussian case (not shown).

Table 3. Statistics of errors (all segments) using nonlinear filters on data from a medium-grade IMU with uniformly distributed errors and with 1 Hz GPS updates (units: cm).

coordinates	UKF		UPF	
	avg.	std. dev.	avg.	std. dev.
f	0.1	1.9	0.1	1.7
l	-0.02	2.0	-0.1	1.9
h	0.6	2.0	0.5	2.0

To test the efficacy of the particle filter (PF), we considered the following asymmetric probability density (APD) (Komunjer, 2007).

$$f(u)=\begin{cases} \dfrac{d_{a,l}^{1/l}}{G(1+1/l)}\exp\left[-\dfrac{d_{a,l}}{a^{l}}|u|^{l}\right], & if \quad u\le 0, \\ \dfrac{d_{a,l}^{1/l}}{G(1+1/l)}\exp\left[-\dfrac{d_{a,l}}{(1-a)^{l}}|u|^{l}\right], & if \quad u>0, \end{cases} \tag{36}$$

where $0\le a\le 1$, $l>0$ and $d_{a,l}=\dfrac{2a^{l}(1-a)^{l}}{a^{l}+(1-a)^{l}}$. If $a=0.5$, then the density is symmetric. If, in addition, $l=2$, the APD is the Gaussian density. For our tests, we chose $l=2$ and two values $a=0.25, 0.75$ (Figure 7), one for the gyro noise, the other for the accelerometer noise. Figure 8 compares the statistics of the position error for the update rates and GPS degradation used in Figure 6, with and without the asymmetry in the IMU sensor noises. We find that both the UKF and EKF performances are significantly degraded in the presence of IMU noise asymmetry; and, moreover, the UKF is not consistently superior to the EKF, especially in the straight sections of the trajectory. Even in the curved sections, the advantage of the UKF seen earlier has been compromised in the case of longer ranging gaps and a degraded GPS solution.

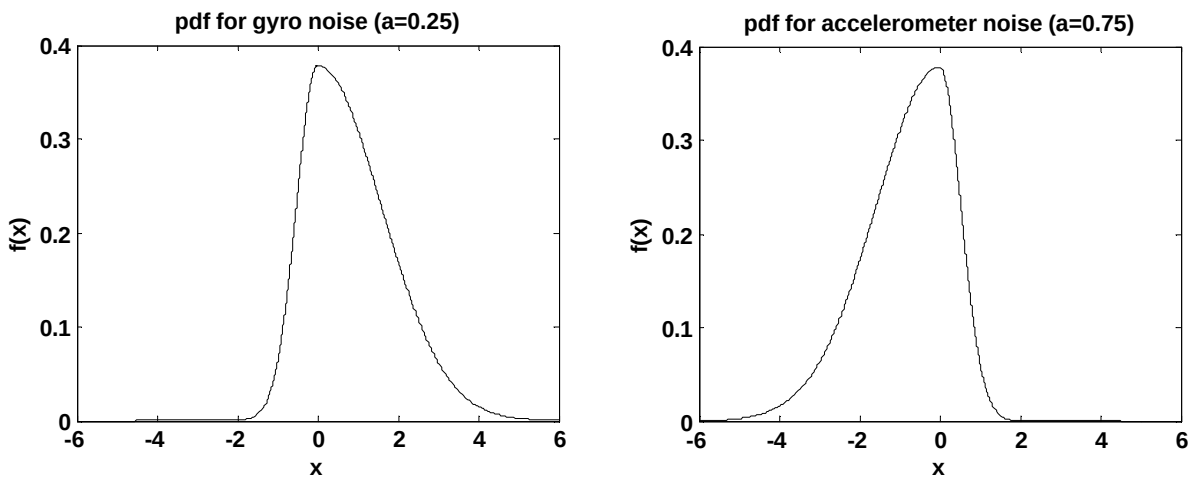

Figure 7: Asymmetric pdf's used for gyro noise ($l = 2$, $a = 0.25$) and accelerometer noise ($l = 2$, $a = 0.75$).

On the other hand, the unscented particle filter (UPF) applied to the IMU data corrupted by the asymmetric noise exhibited (Figure 9) consistently superior performance, both for the curved and the straight segments of the trajectory. This is an interesting result because the UPF still uses the unscented Kalman filter before the re-sampling of the particles; yet, the results are better than for the UKF, alone.

Figure 9 also shows that increasing the number of particles does not yield significant improvements in the UPF. However, by incorporating the adaptive algorithms we further enhance the filter, at least for the longer GPS outage, because the AUPF compensates for the unfulfilled assumptions of the unscented transformation, specifically, that it assumes a Gaussian (at least symmetric) error distribution. The overall positioning accuracy deteriorates as the GPS update interval increases (e.g., 5 s). For example, the standard deviation in position using the UPF with asymmetric error distribution is worse than that of the UKF with symmetrically distributed errors. However, the UPF still performs better than the other filters when the sensor noise is asymmetric.

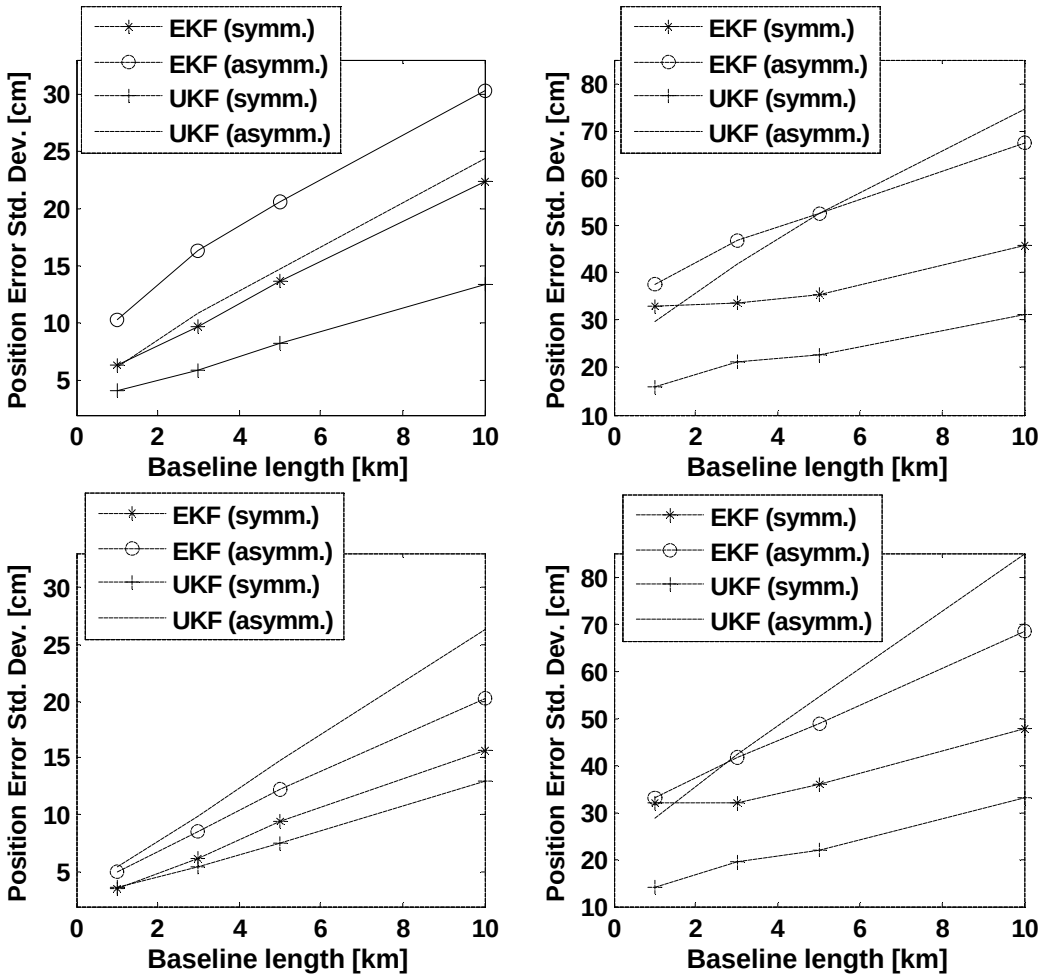

Figure 8: Standard deviation of medium-grade IMU position errors with asymmetric sensor error distributions, for baseline-degraded GPS updates (first row: curve segments, second row: straight segments, first column: 1 s updates, second column: 5 s updates).

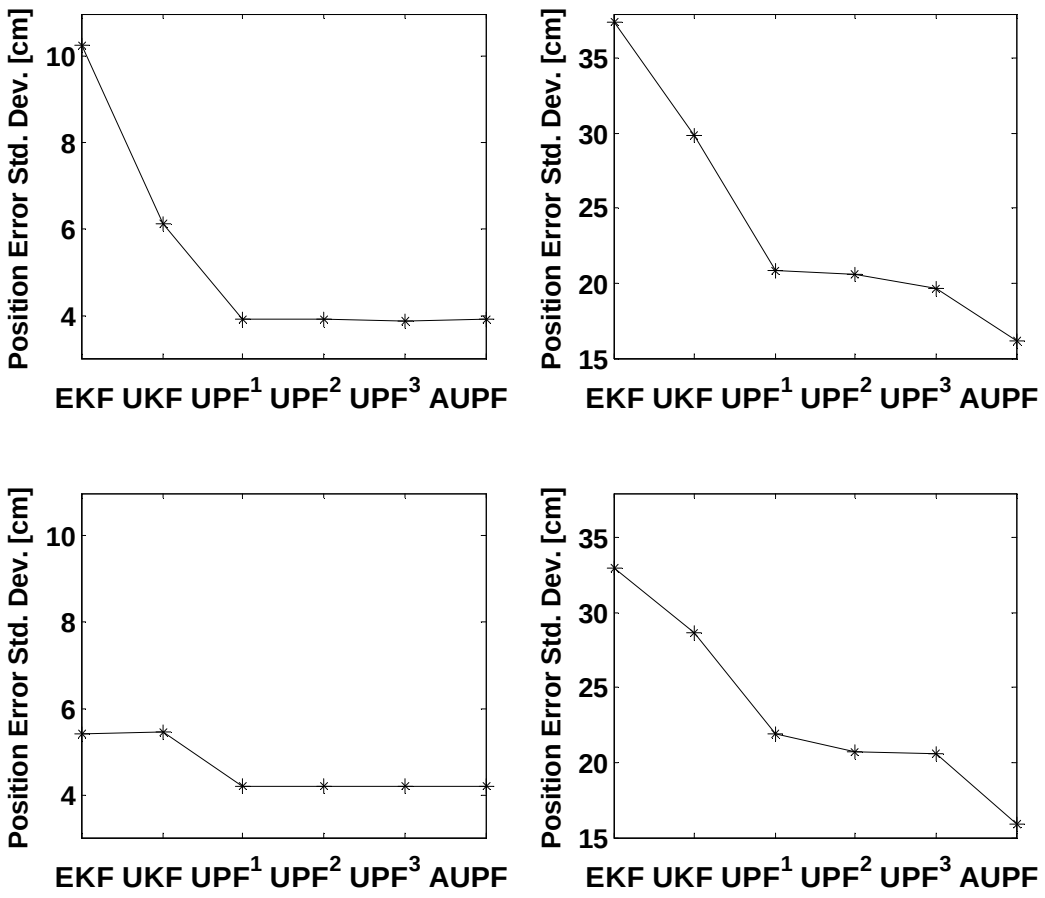

Figure 9: Standard deviations of medium-grade IMU position errors (first row: curved segments, second row: straight segments) for EKF, UKF and UPF with 1 s GPS updates (first column) and for EKF, UKF, UPF^1(200), UPF^2(400), UPF^3(600), AUPF(200) with 5 s updates (second column). The number in parenthesis is the number of particles. GPS update accuracy is for the 1 km baseline (Table 2) and the IMU sensor noise is assumed to be asymmetric as in Figure 7 (units: cm).

4. Performance Using IMU Data

As part of this project we purchased two medium grade IMUs, the HG1900 and the HG1700, from Honeywell, Inc. The HG1700 (Figure 10a) is a light-weight and low-cost ring-laser-based strapdown IMU designed for navigation purposes especially for missile guidance and unmanned vehicles (UAV). The HG1700 includes three miniature GG1308 Ring Laser Gyroscopes (RLGs) and three RBA-500 Resonating Beam Accelerometers. The Honeywell HG1900 (Figure 10b) is a MEMS (micro-electro-mechanical system) based IMU used for the same purposes as the HG1700, but slightly less accurate. It contains MEMS gyros and also RBA500 accelerometers. A comparison of the technical specifications of these two units is provided by the manufacturer in Figure 11.

Figure 10: a) HG1700 IMU, b) HG1900 IMU.

Parameter	Units	HG1700	HG1900
Volume	in^3	33	17
Weight	lbs	<2	<1
Power	Watts	<8	<2
Non-Operating Shock	g max	<500	<500
Gyro Performance			
Parameter	**Units**	**HG1700**	**HG1900**
Operating Range	°/sec	± 1074	±1000
Scale Factor Repeatability	PPM (1σ)	150	150
Scale Factor Linearity	PPM (1σ)	150	150
Bias Repeatability	°/hr (1σ)	1	<17
Bias (In Run Stability)	°/hr (1σ)	1	<7
Bias Static g Sensitivity	°/hr/g (1σ)		3
Bias g2 Sensitivity	°/hr/g2 (1σ)		0.6
Bias Acoustic Rectification Error (ARE)	°/hr max		10
Quantization	μ rad max	13.47	10
Angular Random Walk	deg / hr max	0.125	0.09
Axis Alignment Stability	μ rad (1σ)	500	80
Axis Alignment Stability (nonorthogonality)	μ rad (1σ)	100	50
Accelerometer Performance			
Parameter	**Units**	**HG1700**	**HG1900**
Operating Range	g	70	70
Scale Factor Error	PPM (1σ)	300	300
Scale Factor Linearity	PPM (1σ)	500	500
Bias Repeatability	m-g (1σ)	1	1
Bias Stability	m-g (1σ)	1	1
Vibration Shift	μ-g Max	500	500
Axis Alignment Stability (nonorthogonality)	μ rad (1σ)	100	100
VRW	(m/s) / hr max	0.22	0.22

Figure 11: Manufacturer specifications for HG1700 and HG1900.

Prior to deploying these IMUs in a geolocation system in the field, we tested them in the laboratory in the static mode for noise characteristics and on a cart for controlled navigation. The geolocation filters were tested both in the laboratory using the moving cart on a predefined trajectory and in the field at a UXO detection test site in collaboration with NRL (Naval Research Laboratory). In addition, we tested a new self-calibration procedure for the IMUs locally in a parking lot using a cart-based system with GPS. The following sections provide the details of these tests.

4.1 Static Laboratory Tests

4.1.1 Test Description

Data from the HG1700 and HG1900 units were collected in the stationary mode (with presumably constant room temperature) for the maximum time allowed by the data acquisition software, 1000 seconds at 100 Hz (this produces 100,000 data records). The units were placed on an isolated pillar in the basement of Mendenhall Laboratory at Ohio State University, which is meant for seismic and gravity instrumentation. Therefore, the units are unaffected by external vibrations during these tests. The data were collected using a run-box and software purchased from Honeywell.

4.1.2 Results and Analysis

The raw data were analyzed by subjecting them (unsmoothed) to a Fourier transform to compute their power spectral density (periodogram). Figure 12 compares the psd's for the HG1700 and HG1900 accelerometers. The oscillations evident in the IMU output (not shown) are clearly indicated by peaks in the psd at 0.02 Hz and possibly 0.04 Hz, corresponding to 50 s and 25 s periods. No such resonances are apparent in the psd's of the HG1900 accelerometer data. Moreover, the HG1900 psd's generally have much lower amplitude at the lower frequencies (less than 1 Hz)

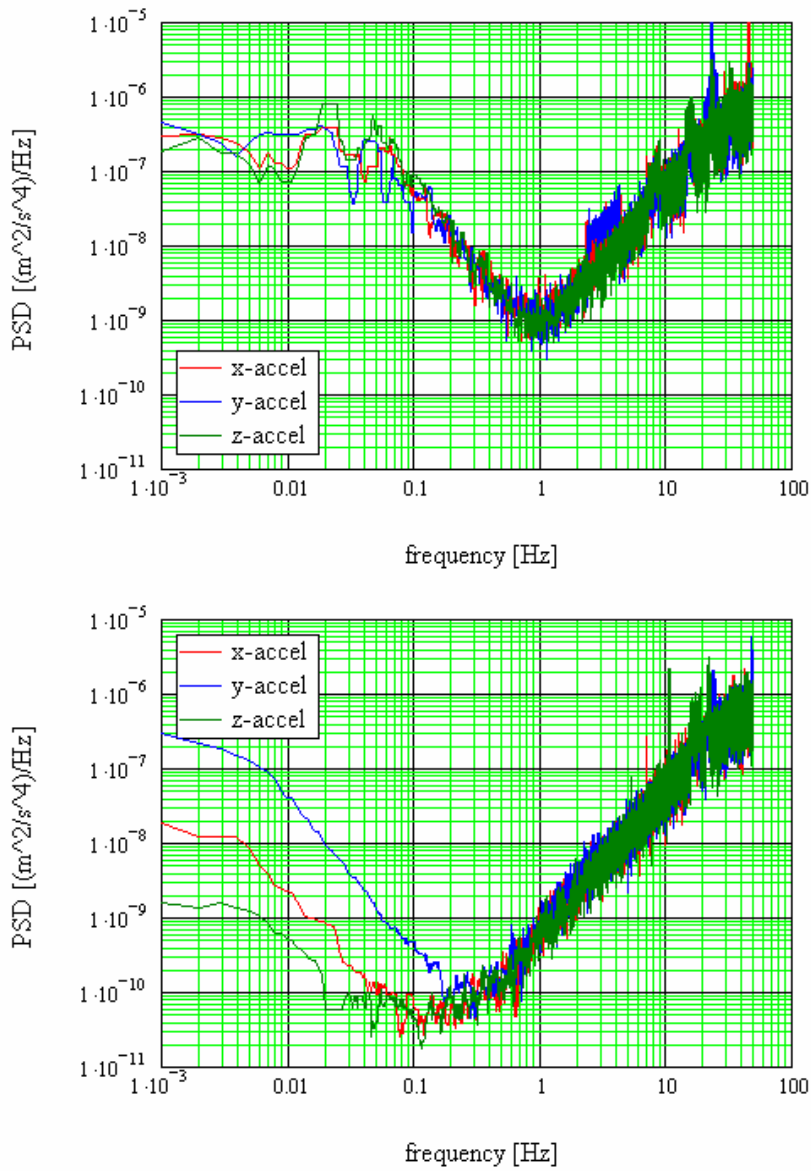

Figure 12: PSD's of the HG1700 (top) and HG1900 (bottom) accelerometers in the static mode.

Similarly, psd's were generated for the gyro data and are plotted in Figure 13. The psd's are similar, although those for the HG1700 have slightly larger amplitude in the frequency band (0.1 Hz – 1 Hz) and significantly greater amplitude for higher frequencies.

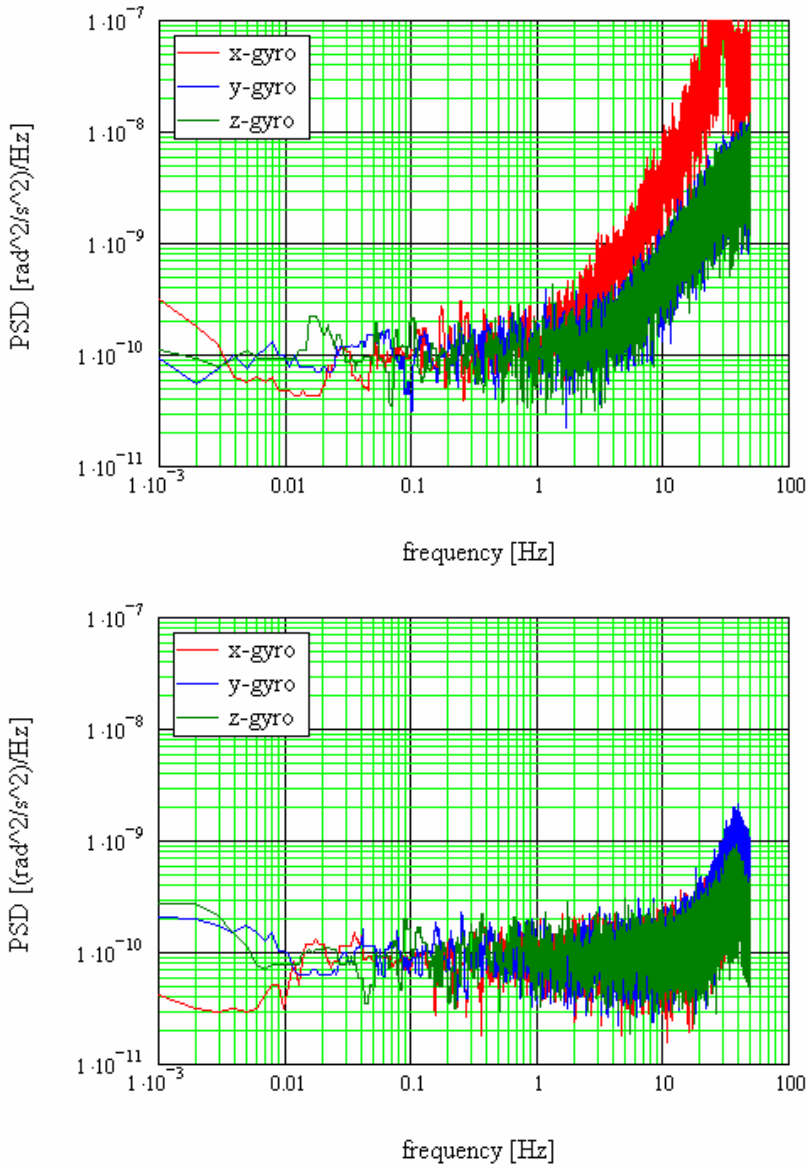

Figure 13: PSD's of the HG1700 (top) and HG1900 (bottom) gyros in the static mode.

Table 4 shows that while both the HG1700 and HG1900 accelerometers fall within specification (Figure 11), the HG1700 accelerometers clearly are noisier. Similarly, for the gyros we find that the HG1700 gyros are slightly noisier (Table 5). However, the gyro biases of the HG1700 (as determined by comparison to Earth's known angular rate) are somewhat lower (also shown in Table 5). Both the biases and angular random walks are within the specifications noted in Figure 11.

Table 4: Noise levels for the IMU accelerometers (static mode).

	white noise	velocity random walk
HG1700 accel	4.8×10^{-4} m/s$^2/\sqrt{\text{Hz}}$	2.9×10^{-2} (m/s)/$\sqrt{\text{hr}}$
HG1900 accel	8.6×10^{-5} m/s$^2/\sqrt{\text{Hz}}$	5.2×10^{-3} (m/s)/$\sqrt{\text{hr}}$

Table 5: Noise levels for the IMU gyros (static mode).

	bias	angular random walk
HG1700 gyro	0.32 °/hr	0.061 °/$\sqrt{\text{hr}}$
HG1900 gyro	–0.76 °/hr	0.039 °/$\sqrt{\text{hr}}$

We conclude that, overall, the HG1700 IMU does not perform as well in the static mode as the HG1900. Nevertheless, when using these units to navigate a cart in laboratory tests (and in subsequent field tests), we consistently obtained slightly better positioning results with the HG1700. The resonances of the HG1700 accelerometers at 0.02 Hz and 0.04 Hz have an unknown origin (the dither of the gyros required to prevent the lock-in phenomenon is likely not the cause since the dither frequency is much higher). Working briefly with the technical staff at Honeywell, we were not able to ascertain the reason for the degraded noise levels of the HG1700.

4.2 Cart-Based Laboratory Tests

We tested the filter/smoothers (AEKF and AUKF), and neural-network aided adaptive filter/smoothers (NN-AEKS and NN-UKS) in the laboratory using the IMUs mounted on a cart. The state vector included three position errors, three velocity errors and three orientation errors associated with the navigation, and a bias and a scale factor error for each of the three accelerometers and the three gyros. For the UKF, four quaternions were employed instead of three angles for the orientation error.

In addition to the two medium-grade IMUs, this cart-based geolocation system (CBGS) also contained the H764G navigation-grade IMU (similar to the LN100 discussed in Section 3.1). In addition, the cart contains the IMU data collection computer hardware and a physical pointer used to identify the cart's passing or occupation of a control point (Figure 14). The pointer served a function similar to an external position observation (such as from GPS). The error specifications of the three IMUs as provided by the manufacturer are described in Table 6. These specified error parameter values are used to generate the initial covariance matrix of the system noise (Q, see equation (4)). The accelerometer bias of the H764G is about 50 times smaller than for the medium-grade units and its gyro biases are similarly much smaller. Although the static tests indicated somewhat poorer noise characteristics for the HG1700, we assigned the manufacturer-specified variances to the Q-matrix and initial P-matrix (for the biases) (see equation (4)).

Table 6: The error specification of three IMUs

		H764G	HG1700	HG1900
Accel Error	Bias	20 µg	1 mg	1 mg
	Scale Factor	40 ppm	300 ppm	300 ppm
	Random Walk	0.003 $(\mathrm{m/s})/\sqrt{\mathrm{hr}}$	0.09 $(\mathrm{m/s})/\sqrt{\mathrm{hr}}$	0.09 $(\mathrm{m/s})/\sqrt{\mathrm{hr}}$
Gyro Error	Bias	0.01 deg/hr	1 deg/hr	<7 deg/hr
	Scale Factor	1 ppm	150 ppm	150 ppm
	Random Walk	0.001 deg/$\sqrt{\mathrm{hr}}$	0.125 deg/$\sqrt{\mathrm{hr}}$	0.09 deg/$\sqrt{\mathrm{hr}}$

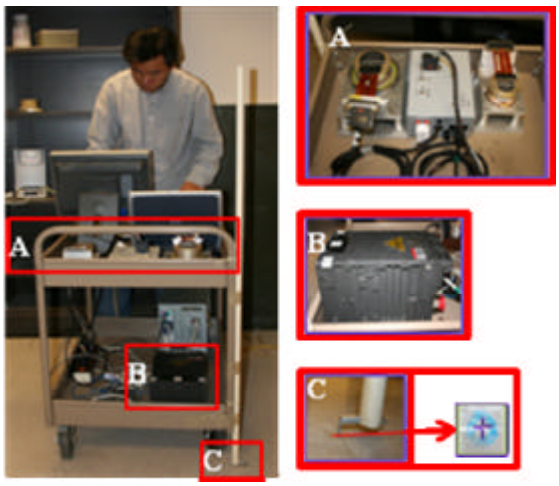

Figure 14: Cart Based Geolocation System, Front (A: HG1700 and HG1900 with run-box, B H764G, C: Pin Point Indicator with Mark)

4.2.1 Test Description

In our laboratory tests, we used simulated position updates (a manual coordinate registration system) instead of integrating the IMU with a ranging system such as GPS. The cart was pushed along a trajectory with pre-defined waypoints that have known coordinates. Whenever the cart passed a particular waypoint, the event was recorded with a timing mark from the computer clock that also time-tagged the collection of data from the IMU. The imperfect recording of the passage of the cart pointer (Figure 14C) over the ground marker could be considered an error in the control point coordinates, although it is a personal error and not as large in magnitude as a kinematic GPS position error. The magnitude of this error is estimated to be less than 1 cm per control point; however, the variance of the measurement error (diagonal matrix, R, see equation (6)) was conservatively set to $(1cm)^2$. The test trajectory had four straight lines and four curved sections (Figure 15). Twenty-eight (28) ground marks were used as "measured" control points for the filtering/smoothing. The distance between points is 12 inches and the CBGS needed about 4 seconds to move from one control point to another. Therefore, the speed of the cart is about 0.076 m/s.

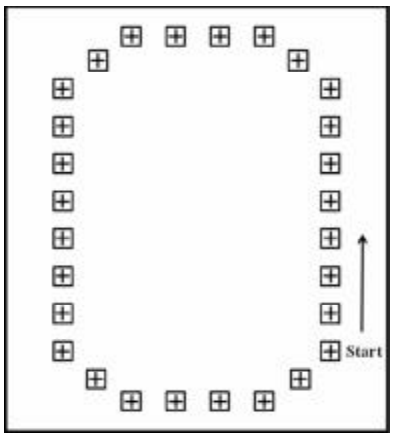

Figure 15: Laboratory test trajectory.

We tested the integrated system by comparing positioning solutions at control points not used in the integration. In the first case, every other point was used to update the system and the filtered/smoothed position estimate was compared to the skipped control. The total duration of inertial positioning between control updates is about 8 seconds in this situation. In the second case, every third point served as update and the estimated positions were compared to the coordinates of the two skipped points. The total simulated GPS outage in this case is about 12 seconds. The (neural-network aided) filtered/smoothed position errors were analyzed along the straight and curved sections, respectively, in terms of the standard deviation of the total 3-D position error computed from 5 separate tests along the same trajectory. In the first case, there are 8 (6) comparison points in the straight (curved) segments, hence 40 (30) comparisons contribute to the standard deviation of the error. In the second case, the corresponding number of comparisons is 45 for both straight and curved segments.

4.2.2 Results and Analysis

Figures 16 and 17 show the standard deviations of position errors of the CBGS according to the different IMUs, the various filtering/smoothing methods, and the interval between control updates. Figures 18 and 19 show the corresponding standard deviations when the neural-network (NN) aided adaptive filter/smoothers were applied. As anticipated, the navigation-grade IMU (HG764G) performs best. Also, the non-linear based smoothing method (AUKS) yields better results than the EKF-based smoothing method, especially in the turning segments. The HG1900 performs only slightly worse than the HG1700. The relative difference in performance between the tactical or medium grade IMUs (HG1700 and HG1900) and the navigation-grade IMU in these tests decreased significantly using the non-linear filtering techniques.

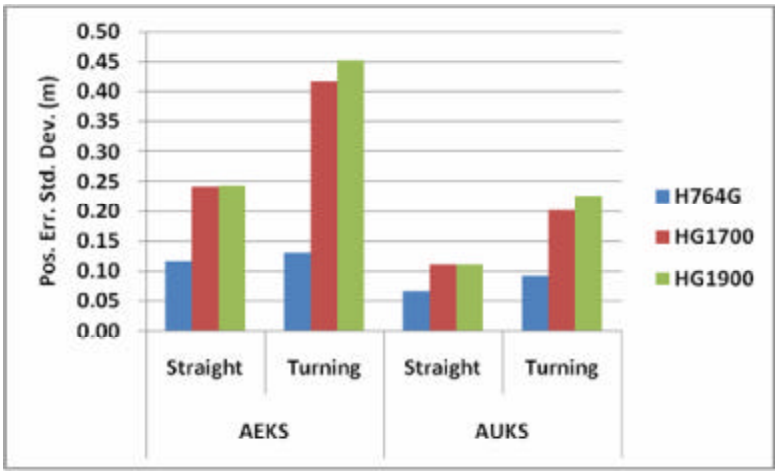

Figure 16: Position Errors of CBGS according to different IMUs and filtering/smoothing methods (control updates every 2 points).

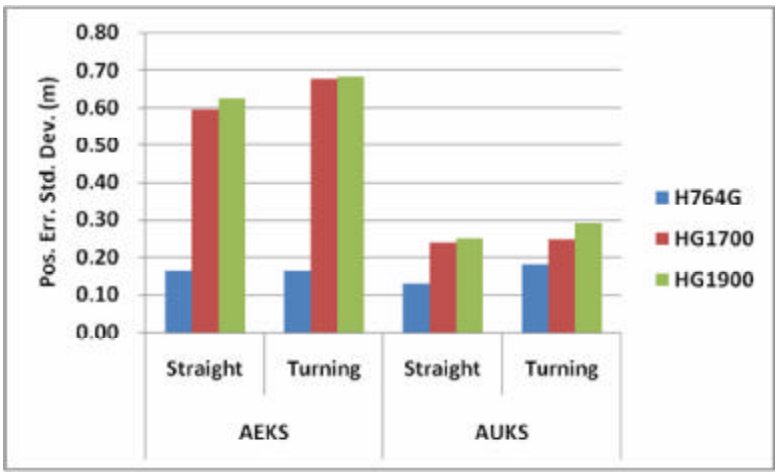

Figure 17: Position errors of CBGS according to different IMUs and filtering/smoothing methods (control updates every third point).

Similar to the two-point update case, in every three-point update case the H764G achieved the best position accuracy; and, the nonlinear, adaptive filter/smoothing techniques demonstrated better performance than the AEKS. However, compared to the first case, there was less difference with both method (AEKS and AUKS) between the straight and turning segments because the accumulation of IMU errors overwhelmed the superiority of the nonlinear filter in a dynamic environment. On the other hand, the non-linear filter still achieves better estimates of states in an essentially non-linear system.

The overall position accuracy was improved by including the neural network aiding, and the disparity in performance between straight and turning sections was reduced. It is noted that the position error of the NN-AEKS decreased dramatically compared to the AEKS in both straight and curved section. The H764G with NN-aided, adaptive filtering/smoothing can achieve the area-mapping position requirement (5 cm) along straight sections with 8 seconds between updates. Similar results were obtained with the longer interval between updates (every third

control point). The position error (st. dev.) of the H764G is less than 10 cm in this case, but in particular, the HG1700 and HG1900 yielded only slightly worse results (1~3cm more in standard deviation). With the increased interval between control points the NN-aided, adaptive filter/smoother was able to maintain the position accuracy better than the unaided adaptive filter/smoother.

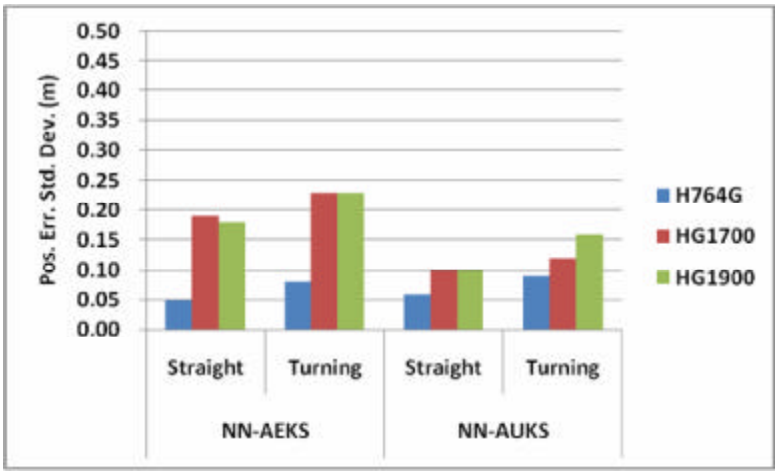

Figure 18: Position Error of CBGS according to different IMUs and NN aided filtering/smoothing method (control updates every 2 points).

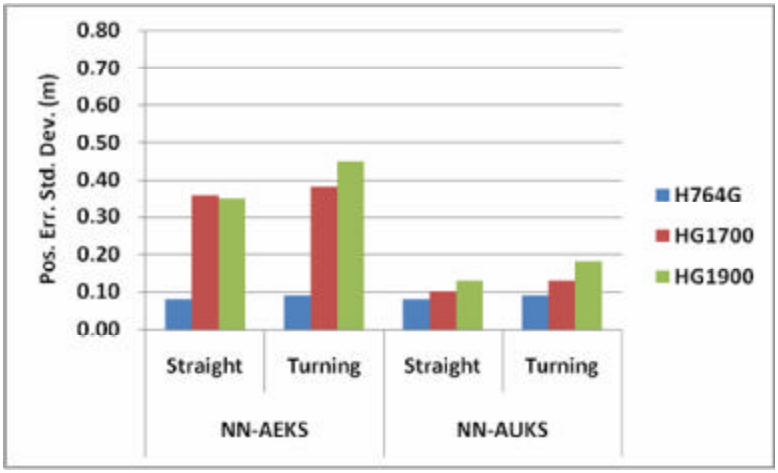

Figure 19: Position Error of CBGS according to different IMUs and NN aided filtering/smoothing method (control updates every 3 points).

4.3 Hand-Held System Tests

The Handheld Geolocation System (HGS) developed for our tests had a tactical-grade IMU (HG1900) and was integrated with an automatic target tracking system that updates its position (Figure 20) at a specified rate. The manufacturer error specifications of the HG1900 are described in Figure 11 and Table 6. A red circle marked on the front head of the HGS was used

as a target that could be tracked for accurate positioning by using real-time color imaging. This external tracked position served the same purpose as would GPS in the field.

In addition, we developed improved software to collect the data from the IMU, thus replacing the Honeywell software (that was an MS-DOS based data acquisition tool) that limited the number of collected data to 100000 records. This also enabled us to collect data using a laptop (replacing the desktop computer used with the cart-based system). The run box obtained from Honeywell still serves as a power and data cable terminal, but otherwise has no function in the data collection.

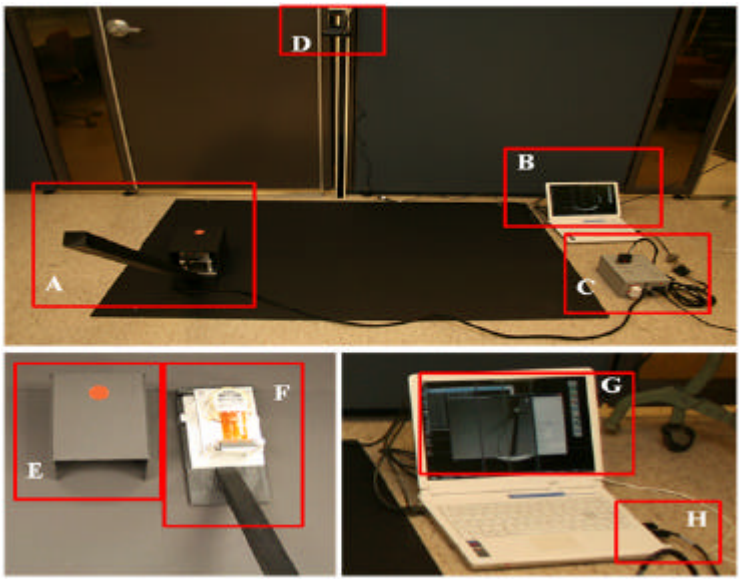

Figure 20. The hardware system for locating geolocation tests (A: Handheld Geolocation System, B: Laptop, C: IMU Run-box, D: Web Cam, E: Target (red dot) with black box, F: HG1900, G: Target tracking software, and H: PCMCIA converter).

In order to obtain accurate positions of the HGS, an automatic target position extraction system was implemented using real-time color imaging with a webcam (at 5Hz update rate). First, the color image is converted to a binary image which has only two values, 0 or 255, for each R, G, and B band (only the R band was employed in this test). Second, the target object in the binary image is extracted from the boundary noise using geometric circularity and knowledge of its size. Finally, the screen coordinates of (the center of the circle) are converted to real world coordinates.

Using our developed target position tracking software the transformed binary image is captured and displayed in the right-top section of the laptop display (Figure 21) with a pre-defined but adjustable threshold value determined with a slide bar. The minimum size of the target and the circularity to differentiate the target from other objects are defined as 100 and 5, respectively. Since the actual map size (128cm*960cm) will be used to convert the target position in the window coordinate system (640×480 [pixel]) to the position in the real-world system, the actual dimension of one pixel is 0.2cm by 0.2cm. The position of image plane of the camera (leveled using bubble levels) and the test area (laboratory floor) are assumed parallel, with the camera located 1 m above the center of the test area. An error of less than 0.5 degree

due to the misalignment between the camera and the test area implies a final position error that is less than 0.87cm ($=0.5^{\circ}\times 1m$, or bout 4 pixels).

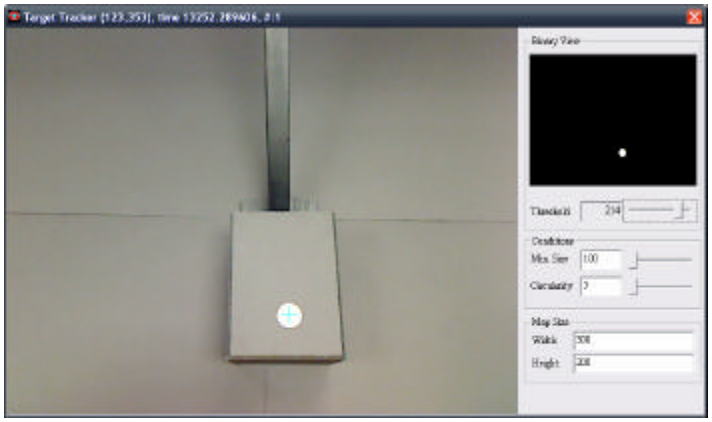

Figure 21. Target position tracking software.

4.3.1 Test Description

The HGS was tested over a small area with its position tracked by the web cam and tracking software, as described in the previous section. The RBPF and the previously developed filters/smoothers (KF/KS and UPF/UPS) were evaluated for typical local trajectories of a hand-held UXO detection system. Without loss in generality, the loosely coupled INS/GPS integration scheme based on the decentralized filter architecture was employed. The state vector for the IMU/imaging system comprised 19 states: two horizontal position errors (dx_N, dx_E) in the navigation frame; two velocity errors (dv_N, dv_E), three orientation errors in a local north-east-down frame (y_N, y_E, y_D); and, biases (b_A and b_G) and scale factor errors (k_A and k_G) for the accelerometers and gyros.

The state vector can be divided using the Rao-Blackwellization described in Section 2.2.3 into two parts according to Nordlund (2002) and Hektor (2007). They argued, based on simulations and airborne test data, that only the position states are highly-nonlinear and all other states can be assumed as linear without significant loss in position accuracy. However, this state division is incorrect in our case because not only the position error states but also the orientation and velocity error states experience high nonlinear dynamics in a ground-based UXO detection system such as the Hand-held Geolocation system. Therefore, the division of states should be separated into the navigation related states (position errors, velocity errors and orientation errors) and all other states (bias and scale factor error of the gyros and accelerometers):

$$\left(x_k^1\right)^T = \left[dx_N \quad dx_E \quad dv_N \quad dv_E \quad y_N \quad y_E \quad y_D\right]^T, \tag{37}$$

$$\left(x_k^2\right)^T = \left[b_{G_N} \quad b_{G_E} \quad b_{G_D} \quad b_{A_N} \quad b_{A_E} \quad b_{A_D} \quad k_{G_N} \quad k_{G_E} \quad k_{G_D} \quad k_{A_N} \quad k_{A_E} \quad k_{A_D}\right]^T. \tag{38}$$

The typical dynamics of a hand-held UXO detection platform can be classified into four categories; linear, curved, sweep, and swing (Bell and Collins, 2007). However, since the linear

and curved sections are included in the sweep and swing dynamics, only two test trajectories (sweep and swing) were considered. The position accuracy of the HGS system was tested along five sweep and five swing trajectories. The sweep trajectory had six straight lines and five curved sections. The swing trajectory had five straight lines and four curved sections. The total distance of sweep (swing) of the trajectory is about 7.2 (5.6) m and the HGS took about 22 (14) seconds to complete total trajectory. Therefore, the speed of the HGS was about 0.33 (0.4) m/s, respectively. Figure 22 shows the trajectories of the first sweep and swing of five separate tests.

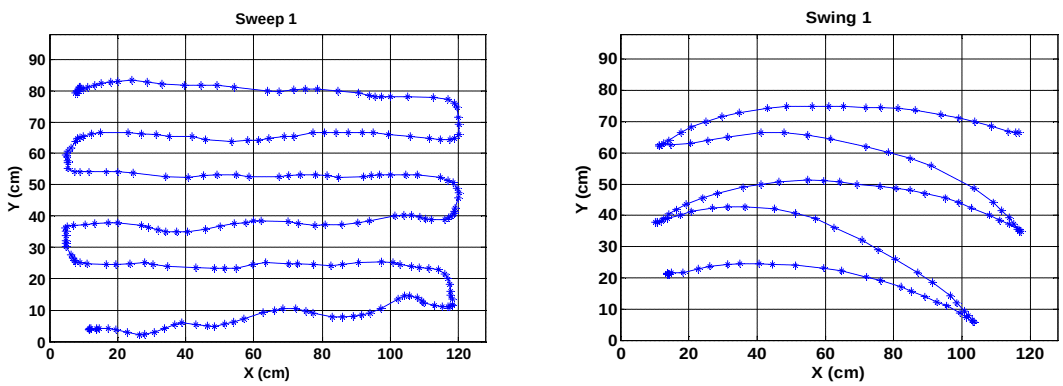

Figure 22. The first sweep and swing trajectory from five tests of the designed handheld UXO Geolocation platform.

4.3.2 Test Results and Analysis

Various update intervals of the imaged target positions were implemented to analyze the filtered/smoothed position estimates with respect to the requirements of position accuracy for MEC geolocation and characterization. In each test case, 5Hz, 2.5Hz, 1Hz, 0.5Hz, and 0.25Hz update rates were employed in the integration. The accuracy of the HGS was tested by comparing the estimated position to the target positions (available at 5Hz) which were not used as updates in the filtering process. For example, if the update rate of the filter is 1Hz, every fifth point of the automatically tracked target position is used as external control (the accuracy of measurement is assumed as 2~4 pixel $(0.4\text{cm})^2$~$(0.8\text{cm})^2$ in north or east direction) in the filter and the other four points are compared to the estimated points of the filter/smoother. The standard deviations of the total 2-D errors (from the EKS, UPS, and RBPS) were computed for the straight and curved sections. The curved section is defined by a pre-defined threshold of absolute value of heading change angle ($\geq 20°$).

Sweep Test: Figure 23 shows the average standard deviations of the error for each of the filters implemented and for each update rate of the control points. The averages represent the results of the five separate sweep tests. In the straight section, the UPS and RBPS can achieve the *discrimination* level of position accuracy (better than 2cm standard deviation) for update rates ranging from 5Hz to a 0.5Hz, and they can achieve the *area mapping* level of accuracy (better than 5cm for standard deviations) at the 0.25Hz update rate. The EKS yields comparable (slightly worse) results at 0.5Hz update rate and significantly worse results when the update rate is 0.25Hz. In the curved section, every filter approached the discrimination level of accuracy (less than 2cm std. dev.) up to 1Hz update rate and achieved 5cm (std. dev.) accuracy at 0.5Hz. The position errors of the RBPF are comparable with the UPS up to 0.5Hz but slightly lower

than all other smoothers at 0.25Hz. Therefore, the RBPS is expected to provide superior performance when the external imaging solution is blocked or degraded for longer than 4 seconds.

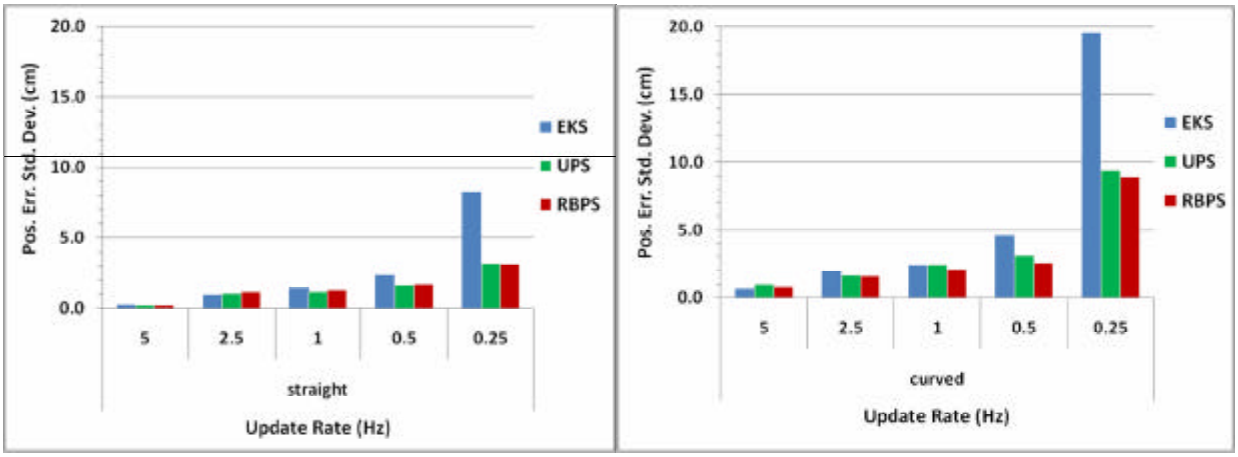

Figure 23. The average standard deviations of position errors according to various smoothing methods (unit: cm) for the sweep tests.

Swing Test: Overall, the results of the swing test were worse than those from the sweep test, especially when the update rate is less than 1Hz. Similar to the sweep test, the non-linear filter/smoothing techniques demonstrated better performance than the EKS. However, compared to the sweep test, there was less of a difference between straight and curved sections in all estimation methods. Figure 24 shows the average standard deviations of position errors according to the various smoothing methods and the update interval between control points. The position accuracy of the swing test was degraded compared to the sweep test, especially when the update rate is less than 1Hz in both straight and curved sections. However, it is noted that the position error of the UPS and RBPS is significantly smaller at 0.25Hz when compared to the EKS in the straight and curved sections.

In the straight section, the UPS and RBPS attained the *discrimination* level of position accuracy up to the 1Hz update rate and achieved the *area mapping* level of accuracy at 0.5Hz update rate (compared to the sweep test where the update rates for the discrimination and area mapping level of accuracy were 0.5Hz and 0.25Hz, respectively). In the curved section, similar to the straight section, the UPS and RBPS achieved the discrimination level up to 1Hz and the area mapping level up to 0.5Hz.

In this swing test, the RBPS performs best at all update rates. Therefore, although the swing operation can obtain position data for the UXO detection in shorter time duration and therefore with fewer control points, the sweep operation is preferred because the position errors of the sweep test were smaller than that of the swing test due to the linear dynamics of the sweep motion.

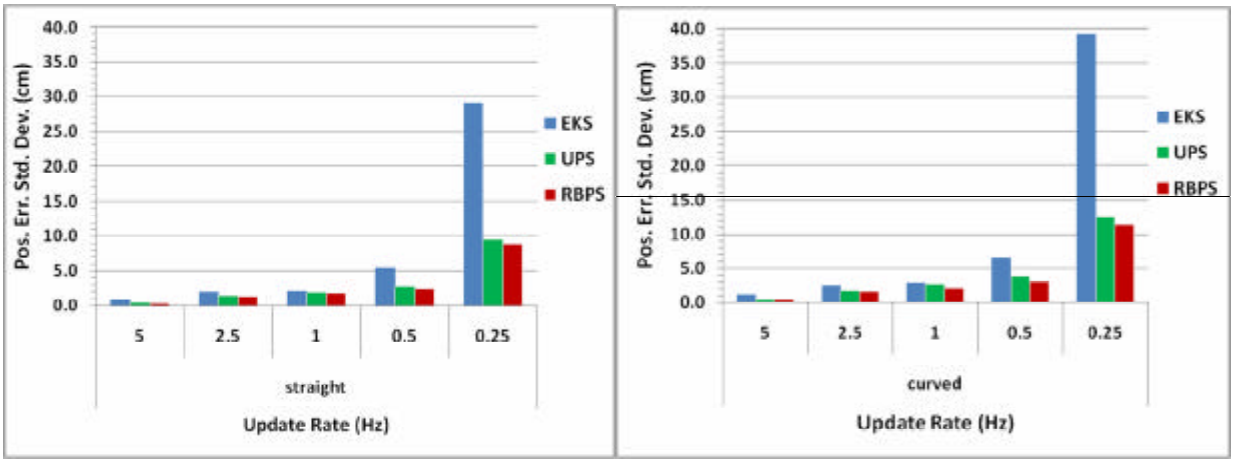

Figure 24. The average standard deviations of position errors according to various smoothing methods (unit: cm) for the swing tests.

The UPS needs at least 200 particles to yield optimal position accuracy in this test. However, the RBPS utilized only 20 samples (particles) for the nonlinear (particle) filter part. Although there is still room for some position accuracy improvement by increasing the number of particles, it will not yield significant improvements (Lee and Jekeli, 2009). Therefore, the RBPS can produce (slightly) better or comparable results compared to the UPS with only 10% of the number of particles used by the UPS.

4.4 Field Tests at NRL Test Facility

The filtering methods described in Section 2 were evaluated using IMU/GPS data from field tests conducted at NRL's UXO test site located at the Army Research Laboratory Blossom Point Facility in Maryland with the Multi-sensor Towed Array Detection System (MTADS, Figure 25a) and a cart-based system (Figure 26). At the center of MTADS we mounted OSU's dual-IMU/GPS system (Figure 25c): two tactical-grade IMUs (HG1700 and HG1900) in the IMU box (Figure 25b), one Topcon geodetic GPS receiver (GB-1000), and a laptop computer for data collection and communication with the sensors. The cart-based system has only OSU's IMU/GPS system and one large 12V battery for power (Figure 26).

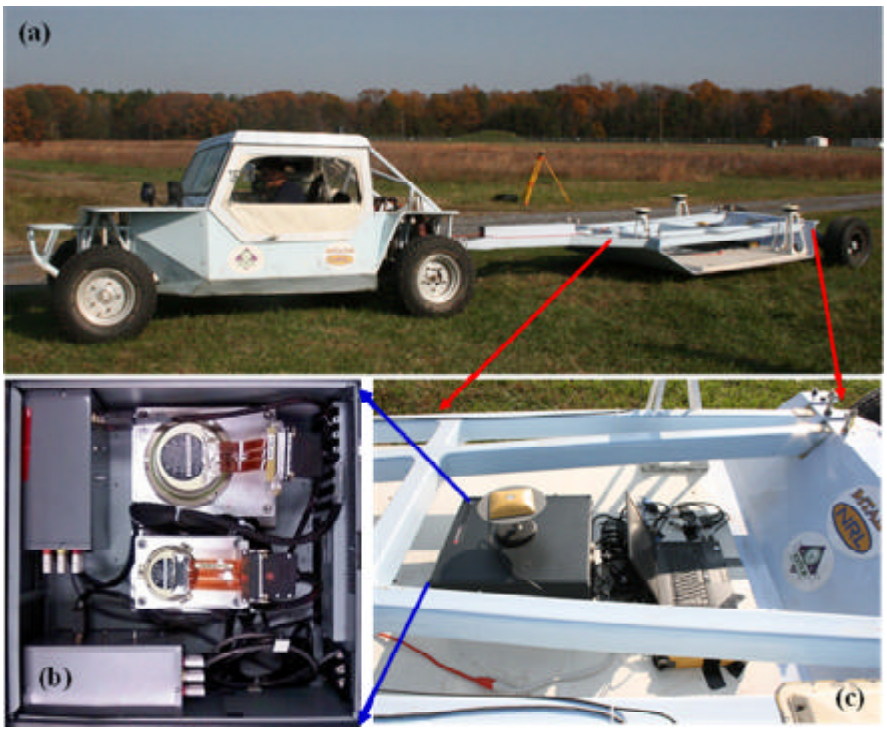

Figure 25. (a) The NRL Multi-sensor Towed Array Detection System (MTADS), (b) IMU box, (c) OSU's dual-IMU/GPS system.

Figure 26. The NRL cart-based system with OSU's dual-IMU/GPS geolocation system.

4.4.1 Test Description

Eight field tests were performed using the two platforms and various GPS satellite configurations. Among these tests, GPS malfunctioned for one complete test, and three tests were designed for deliberate GPS degradation (near a wooded area). Thus, we considered only the four Tests 2, 5, 6, and 7 in this analysis. They were divided into two test scenarios (*Scenario 1*: Tests 2 and 5, *Scenario 2*: Tests 6 and 7) according to the number of visible GPS satellites.

The GPS PDOP (Position Dilution of Precision) for Scenario 1 was lower than that for Scenario 2.

The test range is roughly 84m long by 24m wide. The vehicle-towed trailer and cart-based system were moved along trajectories that are typical of a UXO survey. At the end of each trajectory segment there are large turns to align the platform to the next straight segment of the trajectory.

Figure 27 shows the GPS trajectories of the vehicle-towed trailer and the cart-based system for Scenario 1 (Test 2, MTADS; and Test 5, Cart) and Scenario 2 (Tests 6, Cart, and 7, MTADS). The total distance of Test 2 (Test 5) is about 2,016m (398m) and the speed of the MTADS (Cart) is about 1.85 m/s (0.95m/s). The total distance of Test 6 (Test 7) is about 352m (514m) and the speed of the Cart (MTDAS) is about 1.0 m/s (1.9 m/s).

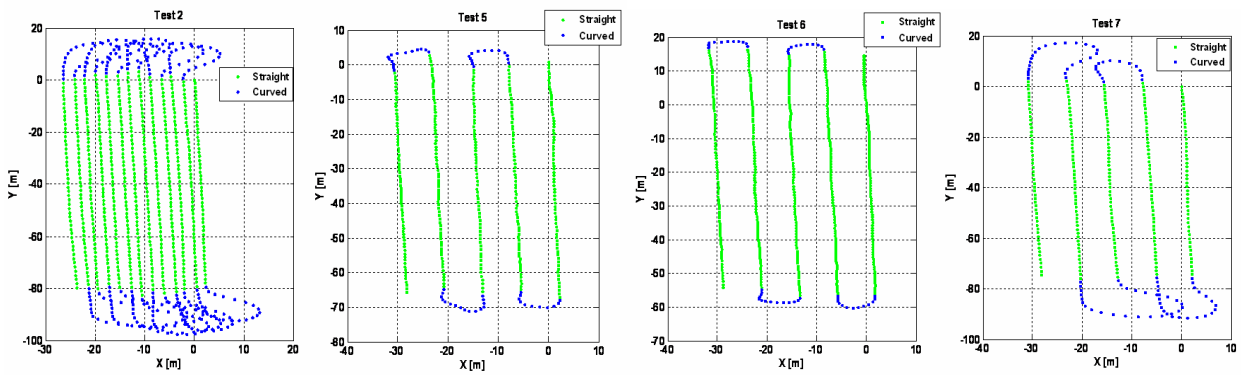

Figure 27. The GPS trajectory of the vehicle-towed trailer and cart-based System (Tests 2 and 5 are Scenario 1 and Tests 6 and 7 are Scenario 2).

The kinematic GPS analysis package "KinTOOLS" was used to process 1Hz GPS data collected by the Topcon GB-1000 receiver. Each trajectory using the individual inertial sensors was estimated by the EKF or the UKF and then the wave correlation filter was applied to the common solutions with the threshold value of 0.5 (equation (30)). The remaining bias and trend errors are further removed by the end-matching method. Figure 28 illustrates the general IMU/GPS data processing and analysis procedure.

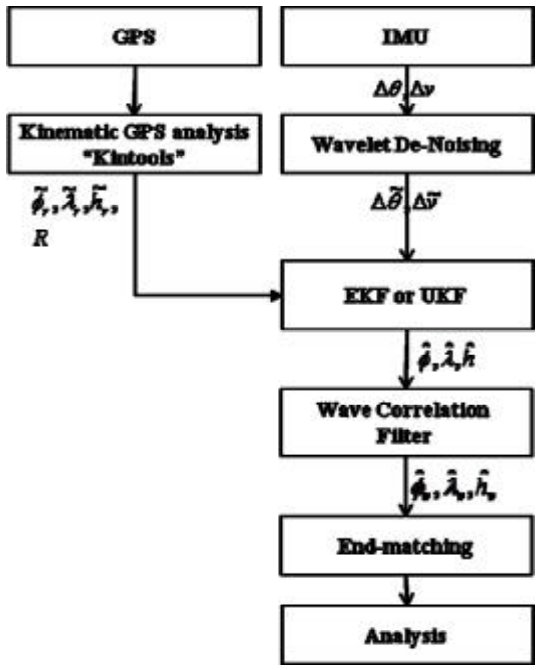

Figure 28. IMU/GPS Data Processing Flowchart

4.4.2 Results and Analysis

Scenario 1: The filtered free-inertial (IMU-only) positions of the vehicle-towed trailer and cart-based system were computed along the straight sections within 2, 4, and 6 second intervals representing artificial periods of GPS unavailability. Figure 29 illustrates parts of the estimated positions from the trajectory of Test 2.

As the interval between GPS updates increases from 2 to 6 seconds, the IMU-estimated position (HG1700) using the EKF with wave correlation filter and end-matching is demonstrably better than the position using just the EKF and the EKF with WCF. Similar improvement was obtained with the WCF applied to the UKF solutions.

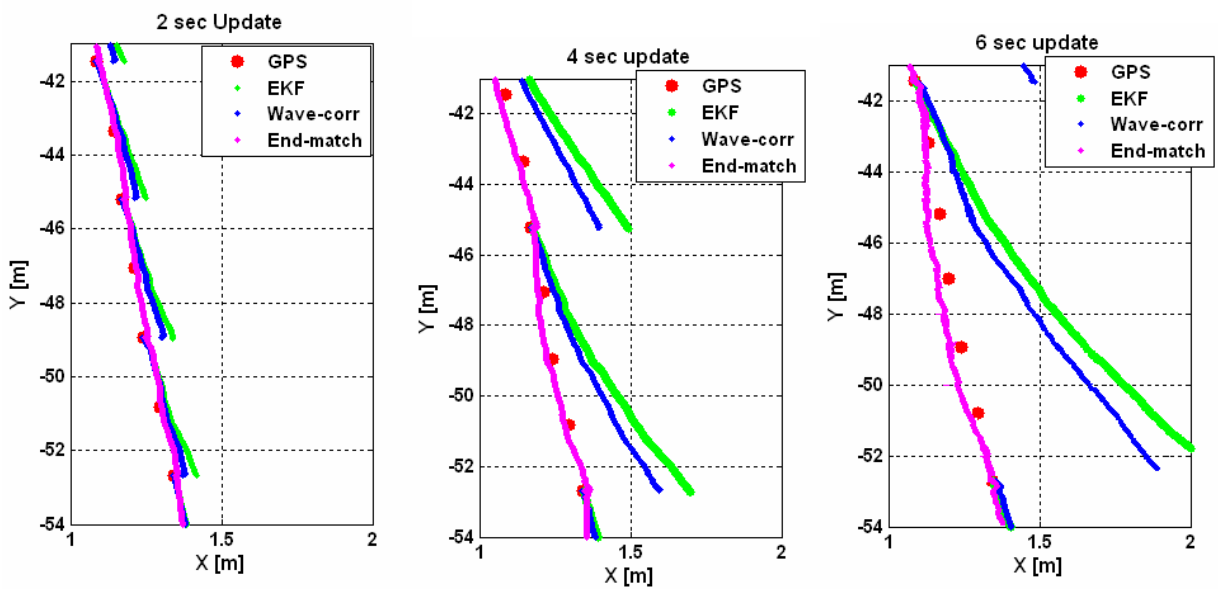

Figure 29. The estimated vehicle trajectory using GPS, the HG1700 w/ UKF the WCF, and end-matching, for different update rates.

Figure 30 shows the standard deviations of position errors of the three coordinates based on all straight sections of the trajectory) of Tests 2 and 5 according to the UKF, the WCF estimates based on the UKF solutions, and the estimates obtained by applying the UKF, the WCF, and end-matching. We show only the UKF-only estimates for the HG1700 because it yields better position accuracy than the HG1900.

Test 5 (cart-based system) yielded overall slightly better performances than Test 2 (vehicle-towed trailer) because the cart-based system experienced lower dynamics and slower speed than the vehicle-towed trailer. The WCF with end-matching improved the UKF solutions (control updates every 2 points) of Test 2 by about 46%, compared to an 11% decrease in the standard deviation of errors without the end-matching.

In the 4 and 6 second GPS outage cases, the position errors (standard deviations) decreased 64% and 76% with respect to the UKF-only errors, and 55% and 70% relative to the UKF with WCF. In Test 5, the position errors with the WCF and end-matching decreased about 52 % ~ 69 % with respect to the UKF-only solutions and 46 % ~ 64 % with respect to the UKF plus WCF solutions, considering all 2, 4, and 6 second GPS outages.

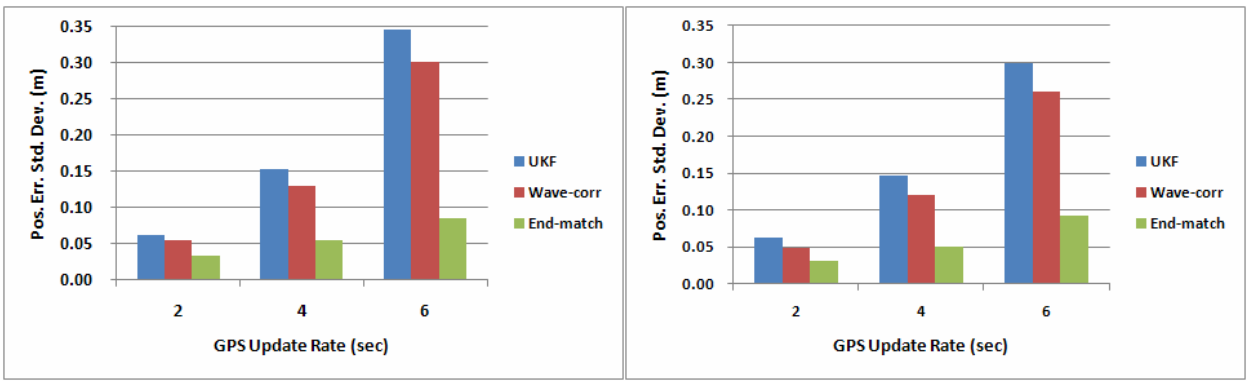

Figure 30. The standard deviation of position error in the straight section according to the UKF, the UKF with WCF, and the UKF with WCF and end-matching based on the UKF solutions (left: Test 2, right: Test 5).

Scenario 2: In Scenario 2 (Tests 6 and 7), the number of GPS satellite increased from 4~5 to 7~8, and the PDOP correspondingly decreased from 4.3 (Test 6) to 2.6 (Test 7). Similar to Scenario 1, the WCF and end-matching improved the performances of the UKF in all straight sections (Figure 31). In Test 6 (Test 7), the position errors with the WCF decreased about 52 % ~ 69 % (50 % ~ 73 %) with respect to the UKF-only solutions, and 44 % ~ 63 % (43 % ~ 67 %) with respect to the UKF with WCF solutions, again considering all GPS outages.

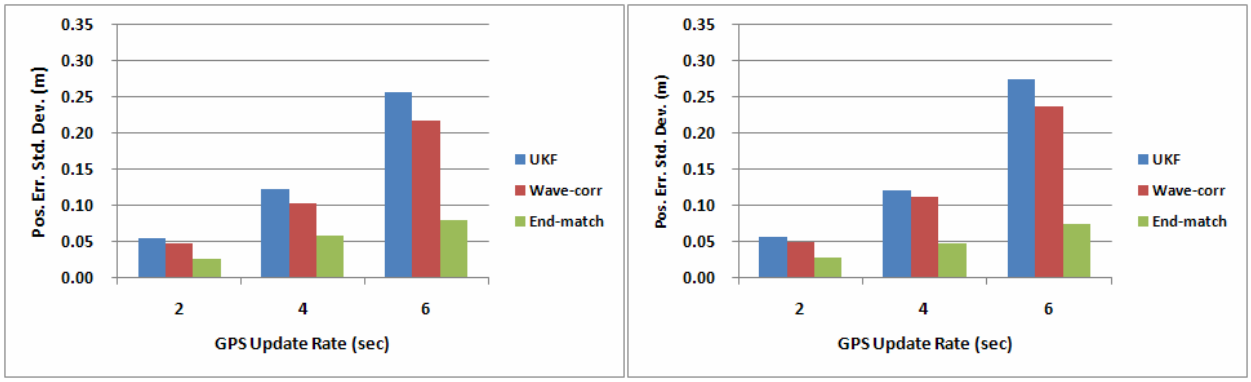

Figure 31. The standard deviation of position error in the straight section according to the UKF, the UKF with the wave correlation filter, and the UKF with the wave correlation filter and end-matching based on the UKF solutions (left: Test 6, right: Test 7).

4.5 Self-Calibration Tests

IMU Calibration is the process of determining the errors in the outputs of the gyros and accelerometers and is essential in order to increase the accuracy of the navigation solution. In the calibration process, the deterministic errors (biases, scale factor errors and sensor non-orthogonality errors) are estimated by comparing the instrument outputs with known data, and the random errors (noise) are minimized by filtering methods. Various kinds of calibration methods for determining the IMU errors have been developed. The most common methods use precise laboratory instruments, but method based on field data can also lead to reasonably accurate calibration, particularly methods

that compare the outputs in the static mode to natural signals generated by the Earth: its gravitational attraction and rotation rate.

We tested the multi-position calibration method developed by Shin (2001) on the two medium level IMUs: HG1700 and HG1900. Because the Earth's rotation rate is relatively weak, some of the systematic errors in the gyros could not be estimated; nevertheless, we assumed a full model of bias, scale factor error, and non-orthogonality for all six sensors of the IMU. The equations for the accelerometer and gyroscope measurements, $\boldsymbol{y}_a$ and $\boldsymbol{y}_w$, respectively, are therefore given by

$$\boldsymbol{y}_a = \boldsymbol{a} + \boldsymbol{b}_a + S_a \boldsymbol{a} + Y_a \boldsymbol{a} + \boldsymbol{w}_a , \tag{39}$$

$$\boldsymbol{y}_w = \boldsymbol{?} + \boldsymbol{b}_w + S_w \boldsymbol{?} + Y_w \boldsymbol{?} + \boldsymbol{w}_w , \tag{40}$$

where $\boldsymbol{a}$ and $\boldsymbol{?}$ are the true acceleration and angular rate vectors; $\boldsymbol{b}_a$, $\boldsymbol{b}_w$, are the respective bias vectors; S_a, S_w, are the scale factor error matrices; Y_a, Y_w are the non-orthogonality error matrices; and $\boldsymbol{w}_a$, $\boldsymbol{w}_w$ are the noise vectors.

For field operations, where the IMU is assumed capable of being oriented in arbitrary directions, we tested the multi-position calibration method developed by Shin and El-Sheimy (2002); see also Syed et al. (2007). By recording the IMU data with different attitudes in the static mode, the deterministic sensor errors are estimated to the extent possible by the natural signals. For a given attitude, the calibration model in the sensor frame for the accelerometers is given by

$$f_a = a_x^2 + a_y^2 + a_z^2 - |g|^2 = 0 , \tag{41}$$

where g is the gravity; and, the true accelerations are, from equation (39),

$$\begin{aligned} a_x &= \frac{y_{ax} - b_{ax}}{1 + s_{ax}} - w_{ax} \\ a_y &= a_x y_{a,yz} + \frac{y_{ay} - b_{ay}}{1 + s_{ay}} - w_{ay} \\ a_z &= -a_x y_{a,zy} + a_y y_{a,zx} + \frac{y_{az} - b_{az}}{1 + s_{az}} - w_{az} \end{aligned} \tag{42}$$

where the notation is self-evident. Similarly, for the gyroscopes the model in the sensor frame is

$$f_w = w_x^2 + w_y^2 + w_z^2 - |w_E|^2 = 0 , \tag{43}$$

where w_E is Earth's rotation rate. From equation (40), we find analogously

$$
\begin{aligned}
w_x &= \frac{y_{wx} - b_{wx}}{1 + s_{wx}} - w_{wx} \\
w_y &= w_x y_{w,yz} + \frac{y_{wy} - b_{wy}}{1 + s_{wy}} - w_{wy} \\
w_z &= -w_x y_{w,zy} + w_y y_{w,zx} + \frac{y_{wz} - b_{wz}}{1 + s_{wz}} - w_{wz}
\end{aligned}
\tag{44}
$$

These models were applied to the outputs for different orientations of the sensor and the error parameters (biases, scale factor errors, non-orthogonality errors) were solved by non-linear least-squares adjustment. For details, see Hayal (2010).

4.5.1 Simulation Tests

The model described in the previous section was tested using simulated measurements of an IMU such as the HG1700 with noise simulated according to parameters given in Table 6. The data were generated by mathematically orienting the sensors relative to the Earth signals with 26 different attitudes, where, imaging the IMU as a cube, each of the 6 faces, 8 corners, and 12 edges in turn was pointed down. Referring to Hayal (2010) for the detailed analyses, these simulations showed that with these measurements, all 9 accelerometer errors (biases, scale factor errors, and non-orthogonality errors) can be estimated accurately (limited only by noise). Also, the gyro biases could be estimated, but it is possible to estimate accurate gyroscope scale factor errors and non-orthogonality errors only if we increase the reference signal strength (e.g., several orders of magnitude greater than Earth rotation) or correspondingly decrease the noise in the data. In this case the bias-only model may be more appropriate. However, our field tests (see the following section) indicated that this may not necessarily lead to better results.

4.5.2 Field Tests

To analyze the multi-position calibration method in the field and how it affects the positioning performance of an integrated IMU/GPS geolocation system, we instrumented a cart with the Honeywell HG1700 and HG1900 IMUs, as well as a GPS receiver (Figure 32), and conducted the appropriate tests in a campus parking lot of the Ohio State University. Initially 20 minutes of warming up time preceded the measurements. As done in the simulations, 26 different 5-minute long static IMU attitude measurements were collected for estimation of the IMU bias, scale factor error and non-orthogonality errors. Then, the IMU box was installed on the cart together with the GPS receiver and the remaining instruments. The GPS measurement and positioning intervals were set equal to 0.1 second. Moreover, another GPS receiver, the base station, was installed at a local control point and its measurement interval was set to 0.1 second. After that, the INS cart was pulled by hand about 25 minutes with a walking speed, and a sweep like trajectory (see Figure 33) was followed among the parking space lines. The trajectory included 25 straight sections and 25 very short and sharp curved sections.

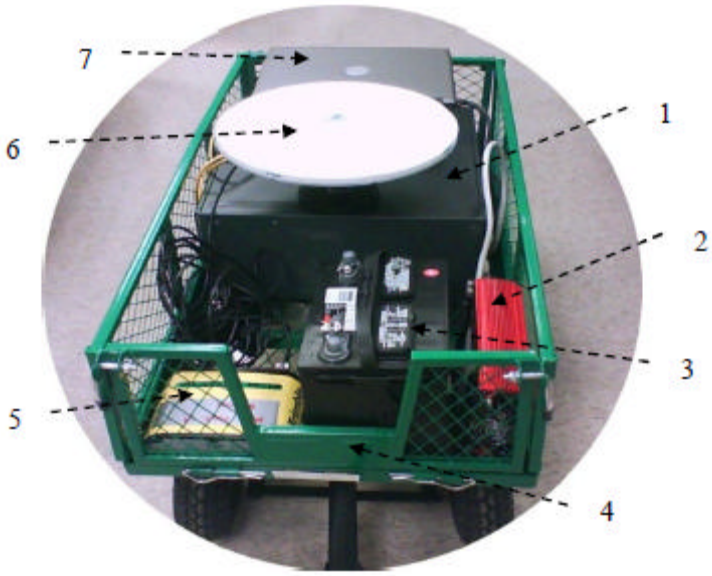

Figure 32: Cart-Based Geolocation System with 1) IMU box containing the HG1900 and HG1700; 2) 120 VAC inverter; 3) 12 VDC battery; 4) hand-pulled cart; 5) Trimble NERTS GPS receiver; 6) Trimble Zephyr Geodetic II GPS antenna; 7) laptop computer, including PCMCI card connecting the IMUs and the decoding software.

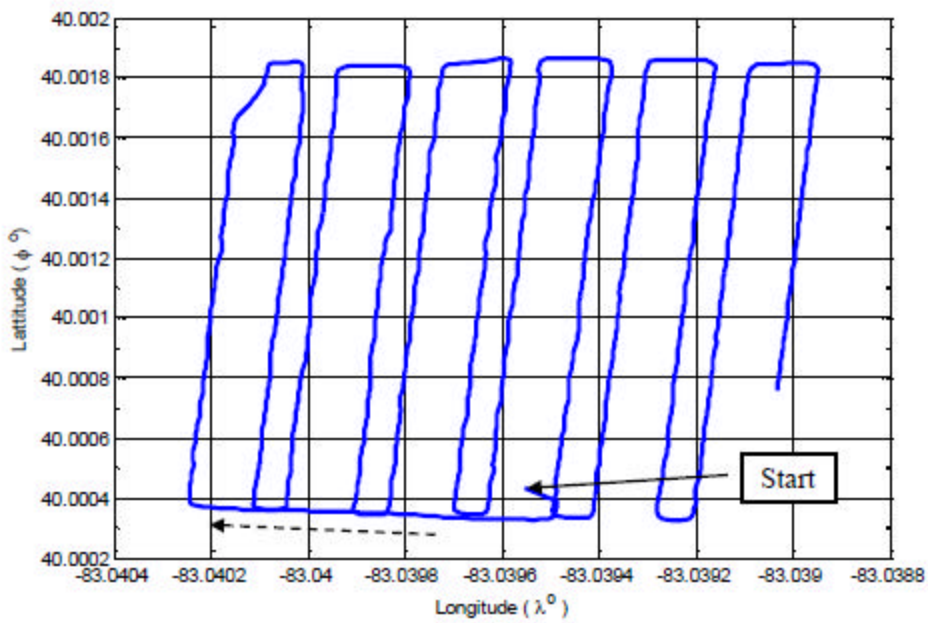

Figure 33: GPS trajectory of field IMU calibration tests.

Various combinations of attitudes (of the 26 available) and parameters (of the 9 for each accelerometer or gyro triad) were tested to determine which scenario would yield the best estimates in the least-squares adjustment. Using just the first 10 attitudes gave the smallest

internal standard deviation in the adjustment for the gyro biases and accelerometer biases, scale factor errors and non-orthogonality errors. This was designated Scenario 3 in the Thesis by A. Hayal (2010). It was the basis for most of the subsequent analysis of the impact of the self-calibration on inertial positioning.

4.5.3 Results and Analysis

The effect on positioning accuracy due to the IMU self-calibration was analyzed using simulated GPS outages along the trajectory of the cart as shown in Figure 33. The estimated gyroscope and accelerometer errors were used as initial estimates in a 27-state Extended Kalman Filter (EKF). Moreover, standard deviations of the initial IMU states were taken from the least-squares solution. Positioning errors and their accuracies were determined by comparing the estimated trajectory during GPS outages to the true GPS trajectory. Aside from the original case which used manufacturer specified initial values for the IMU errors, three field calibration cases were considered, called Scenarios 3.0, 3.3, and 3.9. Scenario 3.0 aimed to test the position accuracy with all 9 self calibrated accelerometer errors, only. Therefore, the chosen gyroscope error parameters were equal to the original case error parameters. Scenario 3.3 included the 3-parameter solution for the gyroscope bias error only, while the use of the 9-parameter solution for all gyroscope errors was designated as Scenario 3.9. The latter was considered even though the scale factor errors and non-orthogonality errors were not well estimated during the self-calibration procedure.

Figures 34 and 35 show the results for the HG1700 and the HG1900, respectively, and for different lengths of GPS outage. We found that it is possible to obtain improved position estimates using all 9 self-calibrated accelerometer errors. Although unrealistic values were obtained for the gyroscope scale factor errors and non-orthogonality errors, the positioning accuracy calculations showed that the full 9-parameter gyro error estimates yielded more accurate results than the 3-parameter solutions for both of the IMUs. The reason for this has not been fully explained, but it also occurs only for the shorter duration of GPS outage (2s). In general, the improvement with self-calibrated errors was most noticeable for the HG1700, while no improvement was realized (in fact, the opposite was the case) for longer GPS outages being supported by the HG1900. This may be due to less stability in the systematic errors for the HG1900. In any case, for longer outages, the use of just the calibrated gyro biases offers generally the best improvement.

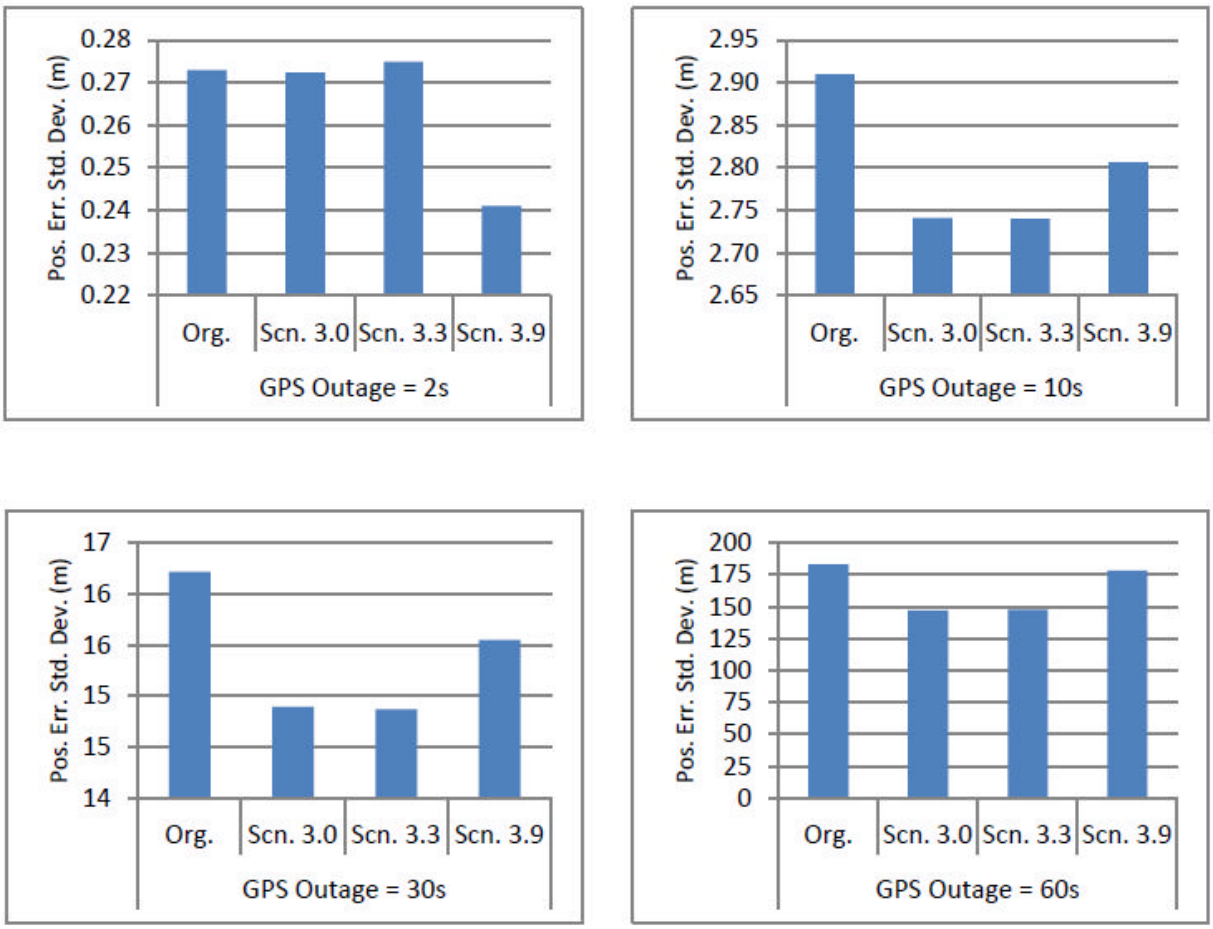

Figure 34: HG1700 inertial positioning errors with self-calibrated IMU errors according to different scenarios (see text) compared to the case without any prior self-calibration prior in the field.

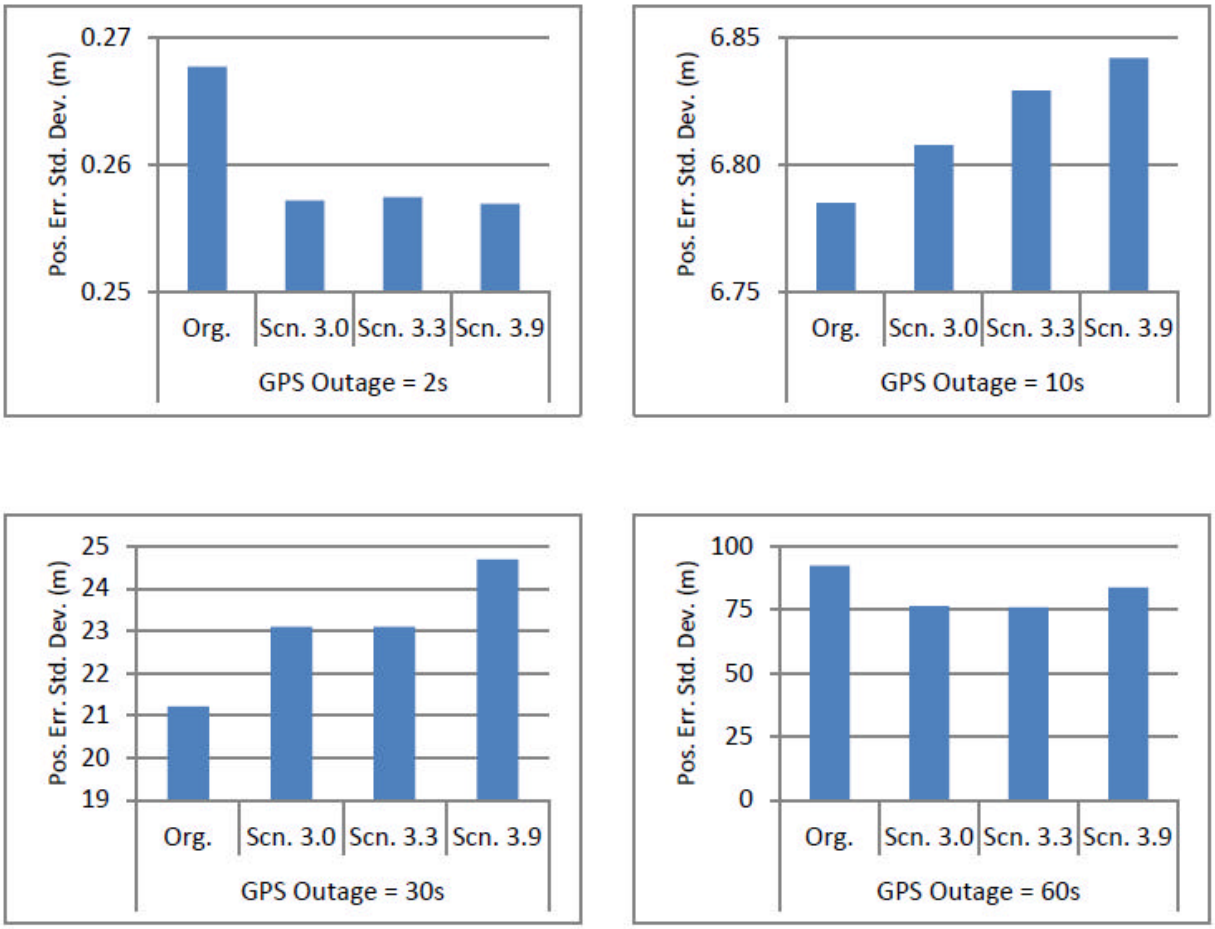

Figure 35: HG1900 inertial positioning errors with self-calibrated IMU errors according to different scenarios (see text) compared to the case without any prior self-calibration prior in the field.

5. Cost analysis

Reliable characterization of MEC requires both high precision and high spatial resolution in the positioning of the detector. For example, Bell (2005) noted that significant improvement and efficiencies could be realized "if a reliable, robust procedure were available for precisely determining the locations of the sensor readings without using the template [method]." GPS generally yields 1 Hz data, which may be inadequate for detectors that pass over smaller putative MEC with speeds of several cm/s or more. One solution is to build a geometrically distributed array of detectors that simultaneously passes over an object (Nelson and McDonald, 2001). Also, laser ranging can deliver up to several 10s Hz resolution (Leica Geosystem[1]), but a ranging system aided by inertial measurement units (that provide high resolution, usually up to 250 Hz) was deemed in a recent study (U.S. Army Corps of Engineers, 2006) as offering the most efficient positioning system in terms of resolution and precision. This synergy of ranging and autonomous inertial sensor systems also mitigates various degrading effects caused by loss of line-of-sight, multipath, and electromagnetic interference.

Our cost analysis is restricted to the expense of determining precise positions with high resolution. The analysis is limited to tangible startup and recurring costs and is based on manufactured product costs and estimated labor costs. There are numerous more or less intangible costs that can only be ascertained with field experience for any particular system. These include the change in cost with a change in the rate of false alarms (which does not exclusively depend on geolocation precision), the differential costs associated with operating in different types of environment, and the various costs of remediation of different categories of MEC in diverse environments.

Another important intangible aspect of the analysis is the operational complexity associated with a particular type of terrain to be surveyed. All geolocation systems depend on an external reference; that is, no system (of reasonable technology and cost) can operate autonomously with the kind of accuracy needed for initial screening, mapping, and discrimination and characterization of MEC. The type of terrain and environment dictates the accessibility and, more importantly, the degree of sustained access to such external references. As in many cases of comparative analyses of different system there are tradeoffs to which costs may or may not be particularly sensitive. Ultimately, we argue that for any geolocation system the inclusion of an IMU is a cost-effective enhancement, if only a safeguard, for precision positioning of MEC detectors.

We compare three competing systems that offer high-resolution positioning in a variety of possibly GPS-degraded environments. The system that is the basis of our analysis for this project is the integrated GPS/IMU geolocation system, comprising a geodetic quality GPS receiver (and antenna) and a medium-grade IMU (such as the Honeywell HG1700 or HG1900). Another external positioning system is the laser-based system whereby the roving (detection) system is positioned using trilateration and triangulation with respect to a number of fixed ground stations occupied by laser-distance measuring devices (robotic total stations). The third system is an acoustic system, where distances are measured between an ultrasonic signal transmitter on the geophysical sensor unit and several stationary receivers in the field. In essence, all external positioning systems can be thought of as a number of benchmarks with known positions transmitting (receiving) a signal to (from) the roving target, which either

[1] http://www.leica-geosystems.com/

through active or passive participation leads to a determination of its position in a well defined coordinate system. With the ground laser trilateration system, the benchmarks are stations in the field and the roving detection system passively reflects the transmitted laser pulses; with GPS, the benchmarks are the satellites that transmit their position and time continuously and the roving system receives and utilizes these signals to determine its position.

In all cases, the line of sight between the benchmark (satellite) and the roving detection system must be unobstructed for the particular wavelengths of the electro-magnetic radiation on which the positioning system is based. Therefore, in principle, the IMU could serve as an aid to each ranging system in the event that the line-of-sight (or acoustic range) is temporarily obstructed, interrupted, or degraded because of various environmental factors. However, for comparison purposes, we assume that the GPS degradation is the most common and serious, since the other ranging systems are ad hoc systems designed specifically for the application in a particular environment. GPS, on the hand, would be considered a viable system in any environment that yields at least a reasonable access to the satellite signals. In that sense an integrated GPS/IMU may be compared to the other stand-alone ranging/geolocation systems.

Table 7 summarizes the basic features of three representative geolocation systems as proposed or realized as described in the final report by the US Army Corps of Engineers (2006), and as studied by us. All three systems rely on GPS or equivalent to perform absolute positioning. The principal innovation is in precision relative position of the UXO detection system. The systems differ in operational principle, where the roving unit for the GPS/IMU and the ultrasonic systems contain the main geolocation sensors, while for the robotic laser-tracking system the principal equipment is a stationary tracking device. As such the costs are not comparable in a direct way. While the GPS/IMU system is completely mobile, the laser tracking system is restricted to the range of the total station, until it can or must be moved (which requires additional manpower). Similarly, other local ranging systems, exemplified by the ultrasonic system require repositioning of equipment at reference station as defined by the survey area.

Table 7: Cost comparison of geolocation systems

System	Component equipment	Cost (ROM estimates)	notes
GPS/IMU	GPS receiver and antenna Inertial Measurement Unit (HG1900)	$29000 $10000	ancillary equipment estimated cost of about $500
Robotic Total Station (RTS)	Laser total station, plus robotic tracking, LeicaTSP1100	$35000	cost for single tracking station; excludes cost of absolute positioning equipment
GPS/ultrasonic ranging	GPS receiver and antenna Ultrasonic units	$29000 $1500	ancillary equipment estimated cost of about $6000

The principal disadvantage of the IMU system for longer-term geolocation is the inherent drift in the navigation solution, which is absent in all ranging systems. For short-term interpolation between reference points (say, less 10 s), the medium-grade IMU with appropriate post-processing performs at levels about an order of magnitude worse than the best ranging

(laser) systems. The main advantage of the IMU is its complete autonomy; requiring no additional base stations and being unaffected by most, if not all environmental conditions.

We showed in our various laboratory and field tests that the HG1700 is the slightly more precise than the HG1900. However, the cost is 60% greater and may not be warranted under most scenarios. Considering the cost of the medium-grade IMU, HG1900, relative to the typical cost of an alternative geolocation system, one may argue that even with the alternative systems, the rover should include an IMU to bridge any possible outages in the ranging system (although most systems claim almost full-time integrity, any ranging system is always susceptible to obstruction or interference). The data processing techniques developed under this project are applicable to the integration of IMU data with any ranging system.

6. Summary and Conclusions

To satisfy precise positioning requirements for MEC detection and characterization, we considered the integrated ranging/IMU geolocation system. Primarily, we studied the algorithms that optimally combine IMU data with updates provided by GPS. Our analysis proceeded from simulations to field data and included various novel estimation tools developed recently for inertial navigation of land and airborne vehicles. We also studied the static self-calibration of systematic IMU errors in the field. The new estimation techniques focused on the non-linearity of the trajectory dynamics and the possible non-Gaussianity of the random instrument errors. Accommodating these characteristics requires more general Bayesian estimation than developed for the extended Kalman filter. Based on simulated trajectories typical of MEC ground surveys, as well as cart-based and hand-held trajectories in the laboratory and actual MEC detection trajectories performed in the field, we analyzed the unscented Kalman filter, the unscented particle filter, a hybridization of these non-linear filters and the extended Kalman filter, known as the Rao-Blackwellized filter, and various modifications, including adaptive error techniques, neural network applications, and wave-correlation filters (for the case the dual IMUs are utilized). We also considered the smoothing version of each of these filters, wherein the estimated IMU trajectory is controlled optimally over the entire inter-update interval by the updates at its endpoints.

Our simulations showed that the unscented Kalman filter (based on the unscented transformation that bypasses a linearization of the error state dynamics and of the observation updates) performs consistently better than the standard extended Kalman filter, particularly along curved trajectories. These improvements in filter strategy were realized especially when the interval of the ranging solution update was several seconds (simulating an outage due to signal occlusions) and if the ranging solution was degraded (simulating various possible causes).

Using particle filters avoids the Gaussianity assumption and our tests showed that these filters are particularly useful if the driving noise of the system has an asymmetric distribution. In this case, the UKF and EKF perform comparably, but the UPF yields significantly improved position accuracy. The UPF results were generally insensitive to the number of particles, and improvement could be obtained (in the case of longer GPS outages) using adaptive techniques that compensated for the UT's assumption of symmetric noise probability densities.

From the various filters tested, we find that achieving few centimeters of positioning accuracy in dynamic environments requires non-linear filters, such as the UKF or UPF. These filters cannot overcome the natural accumulation of IMU errors as the ranging solution update interval increases. However, in all cases the new non-linear filters performed better than the standard EKF. The best performance among all filters tested was obtained by the AUPF which accommodates non-symmetric sensor errors as well as highly dynamic trajectories.

These results were validated using actual cart-based and hand-held IMU trajectories in the laboratory that simulate typical field trajectories. Laboratory tests were conducted using IMUs with different capabilities and along trajectories with different dynamics. The positioning performance was evaluated for linear and non-linear, as well as adaptive and neural-network-aided adaptive Kalman filter/smoothers. As expected, the nonlinear smoothers, developed from a combination of adaptive unscented Kalman filter and RTS smoother (AUKS) yielded superior performance over the standard adaptive extended Kalman smoother. The neural-network aiding, in particular, tended to decrease the *difference* in performance between benign and dynamic components of the trajectory.

A Handheld Geolocation System (HGS) using a tactical-grade IMU was designed to obtain precise positions of a UXO detection system applied in relatively small areas (1.0m by 1.0m). Since the test was operated in a closed environment where no GPS signal was available, an automatic position tracking system was designed and implemented. This would be comparable to GPS if a GPS antenna were mounted on top of the handheld system. As before, the UPF performed generally best among all other (linear and nonlinear) filters. However since the UPF needs a large number of samples to represent the a posteriori statistics in high-dimensional space, the Rao-Blackwellized Particle Filter (RBPF) was tested as an alternative to increase the efficiency of the particle filter. The corresponding nonlinear smoothers that are based on forward/backward filtering techniques (EKS, UPS, and RBPS) were also tested and analyzed for two typical local handheld detection platform trajectories (sweep and swing). On the whole, position accuracy improvements were achieved by applying nonlinear filter-based smoothing techniques (UPS and RBPS) in both the straight and curved sections of the trajectories. The handheld geolocation system with a nonlinear filter-based smoother achieved the characterization and discrimination level of accuracy if the update rate of control points is less than 0.5Hz and 1Hz for the sweep and swing modes respectively. Although the data collection using the swing operation can be done in shorter time, the sweep operation is generally better than the swing because the dynamics of swing operation is highly dynamic.

The improved performance of the IMU/GPS geolocation system using the novel estimation methods was again verified in the field on towed-vehicle and cart-based MEC detection platforms. In collaboration with NRL personnel, we conducted tests at NRL's UXO test site located at the Army Research Laboratory Blossom Point Facility in Maryland. In addition, to the non-linear filters and smoothers, we employed the wave-correlation filter (which, however, requires a dual IMU system), as well as simple endpoint matching as an alternative to the smoothing algorithms. The wave-correlation filter provided only modest improvement, while the endpoint matching yielded similar performance to the smoothing algorithms, due to the relatively benign (straight-line) trajectories that were tested.

Finally, we tested a self-calibration method in the field using our own cart-based geolocation system that included a dual IMU and GPS receiver and antenna. The systematic errors of the inertial sensors could be calibrated in the static mode by orienting their sensitive axes in various directions relative to the Earth's gravity and rotation vectors. In this way biases, scale factor errors, and non-orthogonality errors in the accelerometer outputs were estimated, as well as bias errors in the gyro outputs. It was also demonstrated that these prior calibrations in the field improved the inertial trajectory performance, at least for short (few second) update intervals.

A rudimentary cost analysis of the IMU/GPS geolocation system showed that it is competitive in terms of cost with respect to alternative systems that attempt to improve or aid the standard GPS ranging system. However, the primary function of IMU aiding is more tuned to short-term bridging of GPS outages and providing much higher resolution than GPS can typically offer, similar to or better than laser-tracking systems. IMU aiding is also distinguished by the fact that it requires no external support system and thus is completely autonomous and totally immune to external environmental influences.

Publications reporting the project achievements

1. C. Jekeli and J.K. Lee (2007): Technical Assessment of IMU-Aided Geolocation Systems for UXO Detection and Characterization, Technical Report prepared under contract W912HQ-07-P-0013 for Strategic Environment R&D Program (SERDP), Arlington, VA August 2 2007.
2. J.K. Lee and C. Jekeli (2007): A comparison of filter strategies for precision geolocation of UXO detection instrumentation using integrated IMU systems, *Partners in Environmental Technology Technical Symposium & Workshop*, Washington D.C., December 4-6, 2007.
3. J.K. Lee and C. Jekeli (2008): Nonlinear filter based smoothing methods for MEC detection and characterization using free inertial navigation system, *Partners in Environmental Technology Technical Symposium & Workshop*, Washington D.C., December 2-4, 2008.
4. J.K. Lee and C. Jekeli (2009): The Neural Network and Adaptive Particle Filter for UXO Detection and Characterization using INS/GPS System, ITM 2009 Meeting, San Diego, CA, January 26-28, 2009.
5. J.K. Lee and C. Jekeli (2009): Improved Filter Strategies for Precise Unexploded Ordnance Geolocation using IMU/GPS integration, *Journal of Navigation* 62, 1-18, doi: 10.1017/S0373463309005360.
6. J.K. Lee (2009): Neural network for the precise unexploded ordnance geolocation system. GPS World Tech Talk, 30 Oct 2009, http://techtalk.sidt.gpsworld.com/?p=377.
7. J.K. Lee, A.G. Hayal and C. Jekeli (2009): Handheld Geolocation System (HGS) for UXO Detection and Discrimination Using Low-Cost IMU, *Partners in Environmental Technology Technical Symposium & Workshop*, Washington D.C., December 1-3, 2009.
8. J.K. Lee, Dana J. Caccamise II and Christopher Jekeli (2010): The Precise INS/GPS Geolocation of a Vehicle-towed UXO Detection System, PLANS 2010, May 14~16, 2010.
9. J.K. Lee and C. Jekeli (2010): Neural Network aided Adaptive Filtering and Smoothing for an Integrated INS/GPS Unexploded Ordnance Geolocation System. *The Journal of Navigation*, 63(2), 251-267, doi:10.1017/S0373463309990397.
10. J.K. Lee and Christopher Jekeli (2010): The Double IMU Measurement for the Precise UXO Geolocation System, ION GNSS 2010, Sep. 21 ~ 24 2010, Portland, WA.
11. J.K. Lee and C. Jekeli (2010): Field Demonstration of an Integrated Dual-IMU/GPS for a Precise UXO Geolocation System, *Partners in Environmental Technology Technical Symposium & Workshop*, Washington D.C., Nov 30- Dec 2, 2010.
12. Hayal, A. (2010): Static Calibration of Tactical Grade Inertial Measurement Units. M.S. Thesis, Geodetic Science, Ohio State University, Columbus, OH.
13. J.K. Lee and C. Jekeli (2011): Rao-Blackwellized Unscented Particle Filter for a Handheld Unexploded Ordnance Geolocation System using IMU/GPS, *The Journal of Navigation*, 64, 327–340, doi:10.1017/S0373463310000548.
14. J.K. Lee and C. Jekeli (2011): A Dual-IMU/GPS based Geolocation System. Submitted to *The Journal of Navigation*.

References

Aggarwal, P., Gu, D., El-Sheimy, N. (2006): Adaptive Particle Filter for INS/GPS Integration. ION GNSS 19th International Technical Meeting of the Satellite Division, 26-29 September 2006, pp.1606-1613.

Angermann, M., Khider, M., Robertson, P., Wendlandt, K. (2006), "Continuous location and direction estimation with multiple sensors using particle filtering", 2006 IEEE International Conference on Multisensor Fusion and Integration for Intelligent Systems, pp.92 – 97.

Arulampalam, M.S., Maskell, S., Gordon, N., and Clapp, T. (2001), "A tutorial on particle filters for online nonlinear/non-gaussian bayesian tracking", *IEEE Trans. Signal Process.* 50 (2001) (2), pp. 174–188.

Bell, T. (2001), "Subsurface discrimination using electromagnetic induction sensors", IEEE Trans Geosci Remote Sens 39: 1286-1293.

Bell, T. (2005), "Geo-location Requirements for UXO Discrimination", Presented at SERDP & ESTCP Geolocation Workshop, 1-2 June 2005, Annapolis, MD.

Bell T., Collins, L. (2007), Handheld UXO Sensor Improvements to Facilitate UXO/Clutter Discrimination, SERDP Final Report, Vol 1., Nov. 2007.

Bishop, C.M. (1995), Neural Networks for Pattern Recognition, London, Oxford University Press.

Brown, R.G., Hwang, P.Y.C. (1992): Introduction to Random Signals and Applied Kalman Filtering. John Wiley & Sons, Inc., New York.

Cawsey, A (1998), The Essence of Artificial Intelligence, Prentice Hall PTR

Chiang, K. W. and El-Sheimy, N. (2004), Performance analysis of a neural network based INS/GPS integration architecture for land vehicle navigation, CD proceedings of the 4th international symposium on Mobile Mapping Technology, Kunming, China.

Clynch, J. R. (2001), Lecture note for FUNDAMENTALS OF GEOSPATIAL INFORMATION AND SERVICES, Naval Postgraduate School, Monterey, CA, 2001.

Collins LM, Zhang Y, Li J, Wang H, Carin L, Hart S, Rose-Pehrsson S, Nelson H, McDonald J (2001), "A comparison of the performance of statistical and fuzzy algorithms for unexploded ordnance detection:, Special issue on Recognition Technology, IEEE Trans Fuzzy Systems 9(1): 17-30.

Defense Science Board (2003), Report of the Defense Science Board Task Force on Unexploded Ordnance, Office of the Under Secretary of Defense for Acquisition, Technology, and Logistics, Washington, D.C. 20301-3140, December 2003.

Demuth, H. and Beale, M. (2004): Neural network toolbox for use with Matlab, The MathWorks, Natick, MA.

Doucet, A., de Freitas J.F.G. and Gordon, N.J. (2001), An Introduction to Sequential Monte Carlo Methods, in *Sequential Monte Carlo Methods in Practice,* New York: Springer-Verlag, January 2001.

Farrell J.A., Barth M. (1998), *The Global Positioning System and Inertial Navigation*, McGraw-Hill Publishing, New York, 1998.

Gelb, A. (ed.) (1974), *Applied Optimal Estimation*. MIT Press, Cambridge, MA, 1974.

Godsill, S. J., Doucet, A., West, M. (2000), "Monte Carlo smoothing for nonlinear time series". In Symposium on Frontiers of Time Series Modeling, Tokyo, Japan, 2000, Institute of Statistical Mathematics.

Golden, R. M. (1996), Mathematical Methods for Neural Network Analysis and Design, MIT Press.

Gordon, N., Salmond, D., and Smith, A.F.M. (1993), "Novel approach to nonlinear and nongaussian state estimation", Proc. Inst. Elect. Eng., F, Vol 140, pp. 107-113, 1993.

Gustafsson, F., Gunnarsson, F., Bergman, N., Forssell, U., Jansson, J., Nordlund, P.J., Karlsson, R. (2001): A framework for particle filtering in positioning, navigation and tracking problems. Proceedings of the 11th IEEE Signal Processing Workshop on Statistical Signal Processing, 6-8 Aug. 2001, pp.:34 – 37.

Greenspan, R.L. (1996), GPS and inertial navigation. In *Global Positioning System: Theory and Practice, vol.II*, by B.W. Parkinson and J.J. Spilker (eds.), pp.187-220, American Institute of Aeronautics and Astronautics, Inc., Washington, D.C., 1996.

Grejner-Brzezinska, D. A.(2001), Direct Sensor Orientation in Airborne and Land-based Mapping Applications, 51 pp, June 2001. OSU report 461.

Grewal, M.S., Andrews, A.P. (1993), *Kalman Filtering: Theory and Practice*. John Wiley & Sons, Inc., New York, 1993.

Grewal, M.S., Andrews, A.P. (2001): *Kalman Filtering: Theory and Practice Using MATLAB®*. John Wiley & Sons, Inc., New York.

Ham, F.M. and Kostanic, I. (2001), Principles of Neurocomputing for Science and Engineering, McGraw-Hill.

Hao, Y., Xiong, Z., Hu, Z. (2006), Particle Filter for INS In-Motion Alignment. 1st IEEE Conference on Industrial Electronics and Applications, May 2006, pp.1 – 6.

Hayal, A. (2010): Static Calibration of Tactical Grade Inertial Measurement Units. M.S. Thesis, Geodetic Science, Ohio State University, Columbus, OH.

Haykin S. (1999), Neural Networks: A Comprehensive Foundation (2nd Edition), Prentice Hall, New Jersey, 1999.

Haykin S. (2001), *Kalman Filtering and Neural Networks*, John Wiley & Sons, Inc., New York, 2001.

Hektor, T. (2007), Marginalized Particle Filter for Aircraft Navigation in 3-D, Ph.D. Dissertation, Linkoping University, Linköping, Sweden, 2007.

Honavar, V. and Uhr L. (1994), Artificial Intelligence and Neural Networks: Steps Toward Principled Integration, Boston, Academic Press.

Jekeli, C. (2000), *Inertial Navigation Systems with Geodetic Applications*. Walter deGruyter, Inc., Berlin, 2000.

Jekeli, C., Lee, J.K. (2007), Technical Assessment of IMU-Aided Geolocation Systems for UXO detection and Characterization, Technical Report, August 2007, Strategic Environment R&D program (SERDP), Arlington, VA.

Julier, S.J. (1998), "A Skewed Approach to Filtering", Part of the SPIE Conference on Signal and Data Processing of Small Targets 1998, Orlando. Florida, April 1998.

Julier, S.J., Uhlmann, J.K., Durrant-Whyte, H.F. (1995), "A new approach for filtering nonlinear systems". In Proceedings of the American Control Conference, Seattle, WA, pp.1625-1632, 1995.

Julier, S.J., Uhlmann, J.K. (1996), A general method for approximating nonlinear transformations of probability distributions. Technical report, Department of Engineering Science, University of Oxford, Oxford, England, 1996.

Julier, S.J., Uhlmann, J.K., and Durrant-Whyte, H.F. (2000), "A new approach for nonlinear transformations of means and covariances in filters and estimators", *IEEE Transactions on Automatic Control*, 45(3), 477-482, 2000.

Jwo D.H. and Huang H.C. (2004), "Neural network aided adaptive extended Kalman filtering approach for DGPS positioning", Journal of Navigation, pp. 449-463, 2004.

Kalman, R.E. (1960), A New Approach to Linear Filtering and Prediction Problems. *Trans. of the ASME--Journal of Basic Engineering*, 82, Num. Series D, 35-45.

Kim, D., etc. (2004), "Performance of Long-baseline Real-Time Kinematic Applications by Improving Tropospheric delay Modeling", Proceedings of The Institute of Navigation International Technical Meeting ION GNSS 2004, 21-24 September, Long Beach, California.

Kitagawa, G. (1996), Monte Carlo filter and smoother for non-Gaussian nonlinear state space models, *J. Comput. Graph. Stat.*, vol. 5. Pp. 1-25, 1996.

Klass, M., Briers M., de Freitas N., Doucet, A., Maskell, S., and Lang, D. (2006), Fast particle smoothing: If I had a million particles, in Proc. ICML 2006, Pittsburgh, PA, pp. 481-488.

Komunjer, I. (2007), "Asymmetric power distribution: Theory and applications to risk measurement", Journal of Applied Econometrics, Vol: 22, No: 5, pp: 891-921, 2007.

Korniyenko, O.V. Sharawi, M.S. Aloi, D.N., (2005) Neural Network Based Approach for Tuning Kalman Filter Electro Information Technology, 2005 IEEE International Conference on, Publication Date: 22-25 May 2005, On page(s): 1- 5

Kraft, E. (2003), "A quaternion-based unscented Kalman filter for orientation tracking". Volume 1 of the Proceedings of the Sixth International Conference of Information Fusion, pp.47 – 54, 2003.

Kushner, H.J. (1967), "The dynamics of many physical systems are nonlinear and non-symmetric", Dynamical equations for optimum non-linear filtering, Journal of Differential Equations, 2:179-190, 1967.

Lee, J.K., C. Jekeli, and A. Hayal (2008): Nonlinear Filter Based Smoothing Methods for MEC Detection. Presented at Partners in Environmental Technology Technical Symposium and Workshop, 2-4 December 2008, Washington, D.C.

Lee, J.K., Jekeli, C. (2009), Improved Filter Strategies for Precise Unexploded Ordnance Geolocation using IMU/GPS integration, Journal of Navigation, JULY 2009, VOL. 62, NO. 3, 365–382.

Li, X., Moving Base INS/GPS Vector Gravimetry on a Land Vehicle, vii+144 pp., December 2007, OSU report 486.

Naveau, P., Genton, M.G., Shen, X. (2005), "A Skewed Kalman Filter, Journal of Multivariate Analysis", 2005, 382 – 400.

Nelson, H. H., McDonald, J. R. (2001), "Multisensor Towed Array Detection System for UXO detection", IEEE T. on Geoscience and Remote sensing, Vol. 39, No 6, June 2001.

Nordlund, P.J**.** (2002), Sequential Monte Carlo filters and integrated navigation, Ph.D. Dissertation, Linkoping University, Linköping, Sweden, 2002.

Nordlund, P.J., Gustafsson, F. (2001), Sequential Monte Carlo filtering techniques applied to integrated navigation systems. Volume 6 of the Proceedings of the American Control Conference, 25-27 June 2001, pp.4375 – 4380.

Rauch, H. E., Tung, F., and Striebel, C. T. (1965), Maximum likelihood estimates of linear dynamic systems, *AIAA J.* vol. 3. No. 8, pp. 1445-1450, 1965.

Reddy, G.; Herr, H. (2006), "Using a Gimbal to Calibrate Inertial sensors", Position, Location, And Navigation Symposium, 2006 IEEE/ION, April 25-27, 2006 Page(s):744 – 749.

Rogers, R. M. (2000), *Applied mathematics in integrated navigation systems*. American Institute of Aeronautics and Astronautics, Reston, VA, 2000.

Salychev, O. (1999), *Inertial Systems in Navigation and Geophysics*, Bauman MSTU Press, Moscow, 1999.

Sarkka, S. (2006), Recursive Bayesian Inference on Stochastic Differential Equations. Doctoral dissertation, Helsinki University of Technology Laboratory of Computational Engineering Publications, 2006

Sarkka, S. (2008), Unscented Rauch-Tung-Striebel Smoother, Automatic Control, IEEE Transactions on Volume 53, Issue 3, April 2008 Page(s):845 - 849.

Serpas, J. G. (203): Local and Regional Geoid Determination from Vector Airborne Gravimetry, ix + 105 pp, October 2003, OSU report 468.

Shin, E-H. (2001). Accuracy Improvement of Low Cost INS/GPS for Land Applications, Thesis, UCGE reports Number 20156, The University of Calgary, Calgary, Alberta, Canada.

Shin, E.H. (2005): Estimation Techniques for Low-Cost Inertial Navigation. Ph.D. Thesis, University of Calgary, UCGE Report 20219.

Shin, E-H. and El-Sheimy, N. (2002), A New calibration Method for Strapdown Inertial Navigation Systems, *Z. Vermess.* 127 1-10.

Simon, D. (2006), *Optimal State Estimation: Kalman, H-infinity, and Nonlinear Approaches*, John Wiley & Sons, New Jersey, 2006.

Song, Q. and Han, J.D. (2008), An Adaptive UKF Algorithm for the State and Parameter Estimations of a Mobile Robot, Acta Automatica Sinica, Volume 34, Issue 1, January 2008, Pages 72-79

St-Pierre, M., Gingras, D. (2004): Comparison between the unscented Kalman filter and the extended Kalman filter for the position estimation module of an integrated navigation information system. IEEE Intelligent Vehicles Symposium, 14-17 June 2004, pp.831 – 835.

Syed, Z.F., Aggarwal, P., Goodall, C., Niu, X. and El-Sheimy, N. (2007), A New Multi-Position Calibration Method for MEMS Inertial Navigation Systems, *Measurement Science and Technology*, 18, 1897-1907.

Tarokh, A. B., Miller, E. L. , Won, I. J. and Huang, H. (2004), "Statistical classification of buried objects from spatially sampled time or frequency domain electromagnetic induction data," Radio Science, Vol 39, Np. 4, July/August, 2004, p RS4S05-1-RS4S05-11

Titterton, D.H., Weston, J.L. (2004), *Strapdown Inertial Navigation Technology*. Peter Peregrinus, Piscataway, New Jersey, 2004.

U.S. Army Corps of Engineers (2006), Innovative navigation systems to support digital geophysical mapping ESTCP #200129, Phase III APG demonstrations and Phase IV development. Final Report, 17 February 2006, U.S. Army Corps of Engineers, Engineering and Support Center, Huntsville, AL.

Van der Merwe, R., de Freitas, J. F. G., Doucet, A., and Wan, E. A. (2000), The Unscented Particle Filter. Technical report, Dept. of Engineering, University of Cambridge, 2000.

Van der Merwe, R., Wan, E. (2004): Sigma-Point Kalman Filters For Integrated Navigation. Proceedings of the 60th Annual Meeting of The Institute of Navigation (ION), Dayton, Ohio, June 2004.

Wan, E.A., Van Der Merwe, R. (2001), The unscented Kalman filter. Chapter 7 in: Simon Haykin (Ed.), *Kalman Filtering and Neural Networks*, John Wiley & Sons, New York, 2001.

Wang, J.J.; Wang, J.; Sinclair, D. and Watts, L. (2006), "A neural network and Kalman filter hybrid approach for GPS/INS integration", 12th IAIN Congress & 2006 Int. Symp. on GPS/GNS*S*, Jeju, Korea, 18-20 October, 277-282.

Wang, J.J., Ding, W., & Wang, J., (2007), "Improving adaptive Kalman Filter in GPS/SDINS integration with neural network", 20th Int. Tech. Meeting of the Satellite Division of the U.S. Inst. of Navigation, Fort Worth, Texas, 25-28 September, 571-578.

Yi, Y., Grejner-Brzezinska, D.A. (2006): Tightly-coupled GPS/INS Integration Using Unscented Kalman Filter and Particle Filter. ION GNSS 19th International Technical Meeting of the Satellite Division, 26-29 September 2006, pp.2182-2191.

Zhan R.; Wan, J. (2006), "Neural network-aided adaptive unscented Kalman filter for nonlinear state estimation", Signal Processing Letters, IEEE Volume 13, Issue 7, July 2006 Page(s):445 - 448

Zhang Y, Collins LM, Yu H, Baum C, Carin L (2003) "Sensing of unexploded ordnance with magnetometer and induction data: theory and signal processing", IEEE Trans Geosc Remote Sens 41(5): 1005-1015.